

Linking black-hole growth with host galaxies: The accretion-stellar mass relation and its cosmic evolution

G. Yang,^{1,2*} W. N. Brandt,^{1,2,3} F. Vito,^{1,2} C.-T. J. Chen,^{1,2} J. R. Trump,⁴
 B. Luo,⁵ M. Y. Sun,^{6,7} Y. Q. Xue,^{6,7} A. M. Koekemoer,⁸ D. P. Schneider,^{1,2}
 C. Vignali,⁹ and J.-X. Wang^{6,7}

¹*Department of Astronomy and Astrophysics, 525 Davey Lab, The Pennsylvania State University, University Park, PA 16802, USA*

²*Institute for Gravitation and the Cosmos, The Pennsylvania State University, University Park, PA 16802, USA*

³*Department of Physics, 104 Davey Laboratory, The Pennsylvania State University, University Park, PA 16802, USA*

⁴*Department of Physics, 2152 Hillside Road, U-3046, University of Connecticut, Storrs, CT 06269, USA*

⁵*School of Astronomy & Space Science, Nanjing University, Nanjing 210093, China*

⁶*CAS Key Laboratory for Research in Galaxies and Cosmology, Department of Astronomy, University of Science and Technology of China, Hefei 230026, China*

⁷*School of Astronomy and Space Science, University of Science and Technology of China, Hefei 230026, China*

⁸*Space Telescope Science Institute 3700 San Martin Drive, Baltimore MD 21218, USA*

⁹*Universita di Bologná, Via Ranzani 1, Bologna, Italy*

Accepted XXX. Received YYY; in original form ZZZ

ABSTRACT

Previous studies suggest that the growth of supermassive black holes (SMBHs) may be fundamentally related to host-galaxy stellar mass (M_\star). To investigate this SMBH growth- M_\star relation in detail, we calculate long-term SMBH accretion rate as a function of M_\star and redshift $[\overline{\text{BHAR}}(M_\star, z)]$ over ranges of $\log(M_\star/M_\odot) = 9.5\text{--}12$ and $z = 0.4\text{--}4$. Our $\overline{\text{BHAR}}(M_\star, z)$ is constrained by high-quality survey data (GOODS-South, GOODS-North, and COSMOS), and by the stellar mass function and the X-ray luminosity function. At a given M_\star , $\overline{\text{BHAR}}$ is higher at high redshift. This redshift dependence is stronger in more massive systems (for $\log(M_\star/M_\odot) \approx 11.5$, $\overline{\text{BHAR}}$ is three decades higher at $z = 4$ than at $z = 0.5$), possibly due to AGN feedback. Our results indicate that the ratio between $\overline{\text{BHAR}}$ and average star formation rate (SFR) rises toward high M_\star at a given redshift. This $\overline{\text{BHAR}}/\overline{\text{SFR}}$ dependence on M_\star does not support the scenario that SMBH and galaxy growth are in lockstep. We calculate SMBH mass history $[M_{\text{BH}}(z)]$ based on our $\overline{\text{BHAR}}(M_\star, z)$ and the $M_\star(z)$ from the literature, and find that the $M_{\text{BH}}\text{--}M_\star$ relation has weak redshift evolution since $z \approx 2$. The M_{BH}/M_\star ratio is higher toward massive galaxies: it rises from $\approx 1/5000$ at $\log M_\star \lesssim 10.5$ to $\approx 1/500$ at $\log M_\star \gtrsim 11.2$. Our predicted M_{BH}/M_\star ratio at high M_\star is similar to that observed in local giant ellipticals, suggesting that SMBH growth from mergers is unlikely to dominate over growth from accretion.

Key words: galaxies: evolution – galaxies: active – galaxies: nuclei – quasars: supermassive black holes – X-rays: galaxies

1 INTRODUCTION

The connection between supermassive black holes (SMBHs) and host galaxies is a central topic in extragalactic studies. Observations of the local universe reveal that black-hole mass (M_{BH}) is tightly related to host-galaxy bulge mass

(M_{bulge}) and bulge velocity dispersion (σ) (e.g., Ferrarese & Merritt 2000; Gebhardt et al. 2000; Häring & Rix 2004; Kormendy & Ho 2013). This $M_{\text{BH}}\text{--}M_{\text{bulge}}$ relation suggests that SMBHs and host galaxies evolve in a coordinated way over cosmic history, i.e., the so-called ‘‘SMBH-galaxy coevolution’’ scenario.

The black-hole accretion rate (BHAR) can be inferred from X-ray emission, thanks to the near-universality and

* E-mail: gxy909@psu.edu (GY)

penetrating nature of X-rays generated by the SMBH accretion process (e.g., Brandt & Alexander 2015; Xue 2017). However, since orders-of-magnitude variability is likely common among active galactic nuclei (AGNs) on timescales of $\approx 10^2 - 10^7$ yr (e.g., Novak et al. 2011; Hickox et al. 2014 and references therein), the instantaneous X-ray luminosity (L_X) cannot be used to study the long-term behavior of black-hole accretion. The sample-mean BHAR of a galaxy population is often adopted as a proxy for the long-term average BHAR ($\overline{\text{BHAR}}$, i.e., dM_{BH}/dt).

Much work has focused on relations between $\overline{\text{BHAR}}$ (i.e., the activity of AGNs) and host-galaxy properties such as star formation rate (SFR) and stellar mass (M_\star) in the distant universe. Some studies have found a positive correlation between sample-mean BHAR and SFR, and interpret this result as a reflection of an intrinsic $\overline{\text{BHAR}}$ -SFR relation for individual galaxies (e.g., Mullaney et al. 2012; Chen et al. 2013; Hickox et al. 2014; Delvecchio et al. 2015). In addition, observations have demonstrated that the AGN fraction above a given L_X threshold rises steeply toward high M_\star , suggesting a connection between $\overline{\text{BHAR}}$ and M_\star (e.g., Xue et al. 2010; Lusso et al. 2011; Wang et al. 2017).

The apparent $\overline{\text{BHAR}}$ -SFR and $\overline{\text{BHAR}}$ - M_\star relations might not both be fundamental, because SFR and M_\star are positively correlated through the “star-formation main sequence” for star-forming galaxies. To address this SFR- M_\star degeneracy, Yang et al. (2017) studied the sample-mean BHAR dependence on both SFR and M_\star , and concluded via partial-correlation analyses that $\overline{\text{BHAR}}$ is primarily related to M_\star rather than SFR in general. This result is consistent with some observations suggesting AGN host galaxies have similar SFR as normal galaxies at a given M_\star (e.g., Rosario et al. 2013a; Xu et al. 2015; Stanley et al. 2017; Suh et al. 2017). Therefore, the $\overline{\text{BHAR}}$ - M_\star relation might be a key to addressing questions about SMBH-galaxy coevolution.

Yang et al. (2017) fitted the $\overline{\text{BHAR}}$ - M_\star relation with a log-linear model and found that the slope is consistent with unity (see their Fig. 5). They did not find significantly different $\overline{\text{BHAR}}$ - M_\star relations for the two redshift ranges ($0.5 \leq z < 1.3$ and $1.3 \leq z < 2.0$) used in their analyses. However, the constraints on cosmic evolution were not tight due to the limited sample sizes and large redshift bin widths. Strong cosmic evolution could plausibly exist, since the cosmic BHAR density (ρ_{BHAR}) significantly depends on redshift (e.g., Ueda et al. 2014; Aird et al. 2015). Yang et al. (2017) only probed the $\overline{\text{BHAR}}$ - M_\star relation for galaxies with low and intermediate M_\star [$\log(M_\star/M_\odot) \lesssim 10.5$]. However, massive galaxies may have a very different $\overline{\text{BHAR}}$ - M_\star correlation, due to stronger AGN feedback governing SMBH growth (e.g., McNamara & Nulsen 2007; Anderson et al. 2015).

In this paper, we investigate the $\overline{\text{BHAR}}$ - M_\star relation and its cosmic evolution [$\overline{\text{BHAR}}(M_\star, z)$] over ranges of $\log(M_\star/M_\odot) = 9.5-12$ and $z = 0.4-4$. We do not discuss the $\overline{\text{BHAR}}$ - M_{BH} relation. The $\overline{\text{BHAR}}$ - M_{BH} relation might be more physically relevant than the $\overline{\text{BHAR}}$ - M_\star relation, as high- M_{BH} SMBHs should be more capable of accreting surrounding material. It is even possible that the $\overline{\text{BHAR}}$ - M_\star relation ultimately originates from a $\overline{\text{BHAR}}$ - M_{BH} relation (or other similar relations), since massive galaxies tend to host high- M_{BH} SMBHs. However, unlike M_\star , M_{BH} is not a property of host galaxies, and thus the $\overline{\text{BHAR}}$ - M_{BH} relation does

not directly provide clues about SMBH-galaxy coevolution. Also, M_{BH} measurements are often limited to rare luminous broad-line (BL) quasars and subject to large uncertainties (e.g., Shen 2013). On the other hand, M_\star is an observable for most systems and its measurement techniques are mature (e.g., Santini et al. 2015; Davidzon et al. 2017).

Our $\overline{\text{BHAR}}(M_\star, z)$ is derived from the probability distribution of specific X-ray luminosity [$P(L_{\text{SX}}|M_\star, z)$, where $L_{\text{SX}} = L_X/M_\star$]. The definition of L_{SX} allows it to serve as a rough proxy for the Eddington ratio, i.e., $\lambda_{\text{Edd}} = L_{\text{bol}}/L_{\text{Edd}}$, where $L_{\text{Edd}} = 1.26 \times 10^{38} (M_{\text{BH}}/M_\odot) \text{ erg s}^{-1}$ is the Eddington luminosity and L_{bol} is the bolometric luminosity, as L_{bol} and M_{BH} are broadly correlated with L_X and M_\star , respectively (e.g., Lusso et al. 2012; Kormendy & Ho 2013). For our purpose, choosing the mathematical format of L_{SX} is only to follow the convention of previous work (e.g., Aird et al. 2012; Bongiorno et al. 2012), and the choice of whether to derive $P(L_{\text{SX}}|M_\star, z)$ or $P(L_X|M_\star, z)$ does not affect the final $\overline{\text{BHAR}}(M_\star, z)$. Previous work on $P(L_X|M_\star, z)$ (e.g., Aird et al. 2017a; Georgakakis et al. 2017) focuses on interpreting the physical cause of $P(L_X|M_\star, z)$ itself (e.g., its shape and normalization). Our work utilizes $P(L_X|M_\star, z)$ as a method to derive $\overline{\text{BHAR}}(M_\star, z)$, and study SMBH-galaxy coevolution based on $\overline{\text{BHAR}}(M_\star, z)$. Therefore, our scientific goals are different from those works.

At low and moderate L_{SX} ($\lesssim 1 L_\odot M_\odot^{-1}$), $P(L_{\text{SX}}|M_\star, z)$ has a power-law shape with a slope of $\approx 0.4 - 0.6$ (e.g., Aird et al. 2012; Bongiorno et al. 2012; Jones et al. 2016; Wang et al. 2017). Some recent work identified a sharp drop toward high L_{SX} ($\gtrsim 1 L_\odot M_\odot^{-1}$; e.g., Bongiorno et al. 2016; Aird et al. 2017a; Georgakakis et al. 2017). The break at high L_{SX} is physically expected, because otherwise the average X-ray luminosity ($\overline{L_X}$), which is the integral of $P(L_{\text{SX}}|M_\star, z) \times M_\star \times L_{\text{SX}}$, would diverge.

In this work, we derive $P(L_{\text{SX}}|M_\star, z)$ utilizing the data from CANDELS survey (Grogin et al. 2011; Koekemoer et al. 2011), in particular the GOODS-South and GOODS-North fields (hereafter GOODS-S and GOODS-N), as well as the data from COSMOS survey (Scoville et al. 2007), in particular the UltraVISTA field (McCracken et al. 2012). All these fields have superb multiwavelength coverage. The UV-to-mid-IR (MIR) data allow accurate photometric redshift and M_\star measurements (e.g., Santini et al. 2015; Laigle et al. 2016). All fields have *Chandra* X-ray observations, allowing us to derive L_X for the AGNs. Thanks to the excellent positional accuracy of *Chandra* ($\approx 0.5''$), the matching between X-ray sources and optical/near-IR (NIR) sources is highly reliable, with typical false matching rate less than a few percent (e.g., Xue et al. 2016; Luo et al. 2017). GOODS-S and GOODS-N are small fields ($\approx 170 \text{ arcmin}^2$) but are covered by the deepest X-ray surveys, the 7 Ms *Chandra* Deep Field-South and 2 Ms *Chandra* Deep Field-North (CDF-S and CDF-N; Alexander et al. 2003; Xue et al. 2016; Luo et al. 2017). These two fields provide constraints on $P(L_{\text{SX}}|M_\star, z)$ at low L_{SX} . COSMOS, covered by the COSMOS-Legacy survey, is a much larger field ($\approx 1.4 \text{ deg}^2$ for the utilized UltraVISTA region) than GOODS-S and GOODS-N, although the X-ray data are much shallower ($\approx 160 \text{ ks}$; see Civano et al. 2016). COSMOS generally constrains $P(L_{\text{SX}}|M_\star, z)$ at higher L_{SX} than GOODS-S and GOODS-N. Following Bongiorno et al. (2016), we also constrain $P(L_{\text{SX}}|M_\star, z)$ utilizing the X-ray luminosity function (XLF) and stellar mass func-

tion (SMF) from the literature. This technique can constrain $P(L_{\text{SX}}|M_\star, z)$ for rare high- L_X AGNs which are included in the XLF.

We do not calculate $\overline{\text{BHAR}}(M_\star, z)$ via averaging the instantaneous BHAR from samples of galaxies in surveys (e.g., Yang et al. 2017). Survey data often have small-area effects; e.g., accretion power from rare luminous AGNs is not included due to the limited size of the survey area, and this effect is difficult to determine when performing sample averaging of BHAR. Also, it is challenging to combine different surveys when directly averaging the instantaneous BHAR, because different X-ray data have large differences in sensitivity. However, these issues can be properly considered when modeling $P(L_{\text{SX}}|M_\star, z)$ (e.g., Aird et al. 2012; Bongiorno et al. 2016).

This paper is structured as follows. In §2, we describe the survey data, SMF, and XLF. We detail our analyses and results in §3. In §4, we discuss the implications of our measurements, and summarize our work in §5.

Throughout this paper, we assume a cosmology with $H_0 = 70 \text{ km s}^{-1} \text{ Mpc}^{-1}$, $\Omega_M = 0.3$, and $\Omega_\Lambda = 0.7$, and a Chabrier initial mass function (Chabrier 2003). Quoted uncertainties are at the 1σ (68%) confidence level, unless otherwise stated. We express L_{SX} in units of $L_\odot M_\odot^{-1}$, and M_\star (M_{BH}) in units of M_\odot , unless otherwise stated. L_X indicates AGN intrinsic X-ray luminosity at rest-frame 2–10 keV and is in units of erg s^{-1} .

2 DATA AND SAMPLE

2.1 Multiwavelength Surveys

In this work, we compile observational data from the GOODS-S, GOODS-N, and COSMOS surveys.

2.1.1 GOODS-S and GOODS-N

We include all 34,779 and 34,651 galaxies in the GOODS-S and GOODS-N catalogs, respectively (Grogan et al. 2011; Koekemoer et al. 2011; Guo et al. 2013). In the catalogs, 4,314 and 4,660 sources have $\log M_\star > 9.5$ (our $\log M_\star$ threshold; see §3.2.2). The basic information for these two fields is summarized in Tab. 1. These two catalogs are based on H -band detections with 3σ limiting magnitude of $H \approx 28$. The solid angle is $\approx 170 \text{ arcmin}^2$ for both the GOODS-S and GOODS-N surveys. We utilize both fields to minimize the effects of cosmic variance.

We adopt the galaxies' M_\star and redshift from Santini et al. (2015) and Barro et al. (in prep.), respectively, for GOODS-S and GOODS-N sources. The M_\star and redshift measurements in both fields are based on spectral energy distribution (SED) fitting of broad-band photometry ranging from the U band to *Spitzer*/IRAC bands (i.e., 3.6, 4.5, 5.8, 8.0 μm). In both surveys, the M_\star estimations were performed by several independent teams, some of whom used galaxy templates with nebular emission. The nebular emission is important at high redshift ($z \gtrsim 2$), where some strong emission lines enter the wavelength ranges of the NIR bands. Since this work includes redshifts up to $z = 4$, we adopt the median M_\star of teams using templates with nebular emission;

Table 1. Summary of Survey Data

Name (1)	Area (deg^2) (2)	Galaxies (3)	X-ray Depth (4)	AGNs (5)
GOODS-S	0.05	4,314	7 Ms	264
GOODS-N	0.05	4,660	2 Ms	195
COSMOS	1.38	141,004	160 ks	1,448

NOTE. — (1) Field name. (2) Area of the field in units of deg^2 . (3) Number of galaxies above $\log M_\star = 9.5$. (4) *Chandra* effective exposure time. (5) Number of AGNs with $\log L_{\text{SX}} > -2$.

these median M_\star values are available in the catalogs of Santini et al. (2015) and Barro et al. (in prep.). The SED-based M_\star measurements have typical uncertainties of $\lesssim 0.3$ dex (e.g., Santini et al. 2015). The redshifts are taken from spectroscopic measurements when available; otherwise, they are high-quality photometric redshifts. These photometric redshifts in GOODS-S and GOODS-N have median uncertainties $[|z_{\text{phot}} - z_{\text{spec}}|/(1 + z_{\text{spec}})]$ of 0.02 and 0.004, respectively, and outlier fractions $[|z_{\text{phot}} - z_{\text{spec}}|/(1 + z_{\text{spec}}) > 0.15]$ of 9% and 5%, respectively. The M_\star as a function of redshift is shown in Fig. 1 (top and middle).

We also obtain the SED-based SFR values from Santini et al. (2015) and Barro et al. (in prep.) to classify galaxies as star-forming or quiescent. The SFRs from SED fitting have typical uncertainties of ≈ 0.5 dex (see, e.g., §2.2 of Yang et al. 2017). Although the errors are relatively large, they are sufficient for our purpose (star-forming vs. quiescent classification; e.g., Aird et al. 2017a). We adopt a SFR threshold that is 1.3 dex below the star-forming main sequence (Eq. 1 in Aird et al. 2017a). If a galaxy has SFR above (below) this threshold, we classify it as star-forming (quiescent). We do not classify galaxies hosting a BL AGN, as the total UV flux of these galaxies might have a significant contribution from the AGN thereby biasing the SED-based SFRs.

We cross-correlate these galaxies with the X-ray sources in the CDF-S (Luo et al. 2017) and CDF-N (Xue et al. 2016) surveys using the method described in Yang et al. (2017). CDF-S and CDF-N fully cover GOODS-S and GOODS-N, respectively. They are the deepest X-ray surveys with 7 Ms and 2 Ms *Chandra* observations, respectively. We only use hard-band (observed-frame 2–7 keV) detected sources, taking advantage of the fact that the hard band is less affected by obscuration than the soft band (observed-frame 0.5–2 keV). Soft-band detections are biased to less-obscured sources, and it is difficult to account for this bias with our methodology (see §3.1.1). Also, for a source detected in the soft band but not in the hard band, it is not feasible to obtain their absorption-corrected L_X which is necessary in our analyses (§3.1.1).

We obtain hard-band fluxes from Xue et al. (2016) and Luo et al. (2017) and convert them to L_X assuming a power-law spectral shape with a photon index of $\Gamma = 1.6$ and that absorption only has minor effects on the observed hard-band flux (e.g., Liu et al. 2017; Yang et al. 2017). We justify these assumptions in §3.5.1 and discuss the contamination from X-ray binaries (XRBs) in §3.5.2. We adopt $\Gamma = 1.6$ instead of $\Gamma = 1.8$ – 1.9 , mainly because the former can produce L_X values that agree better with those from X-ray spectral fitting

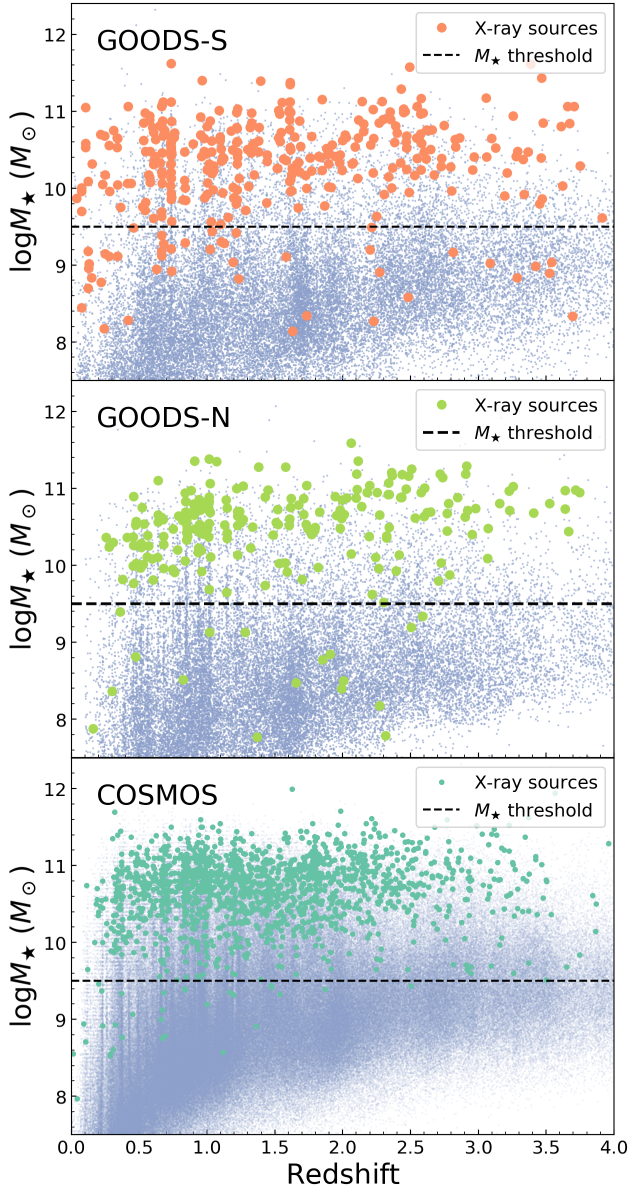


Figure 1. M_* as a function of redshift for GOODS-S (top), GOODS-N (middle), and COSMOS (bottom). The total numbers of galaxies in these three fields are 34,779, 34,651, and 520,778, respectively. The small blue points indicate galaxies; the larger points indicate X-ray-detected sources. The dashed horizontal line indicates our M_* threshold (see §3.2.2).

(see §3.5.1 for more details). Although the observed-frame soft band corresponds to rest-frame energies above 2 keV at $z > 3$, we do not use the soft-band data for high- z sources, as obscuration generally becomes stronger toward high redshift, and the soft band can still be affected by obscuration at high redshift (e.g., Vito et al. 2014b; Liu et al. 2017). Fig. 2 displays the sky coverages as a function of hard-band flux for GOODS-S and GOODS-N, and Fig. 3 shows L_X and L_{SX} as functions of redshift for X-ray detected sources in these two fields. There are 264 and 195 X-ray AGNs with $\log L_{SX} > -2$ (our L_{SX} cut; see §3.2.3) in GOODS-S and GOODS-N, respectively.

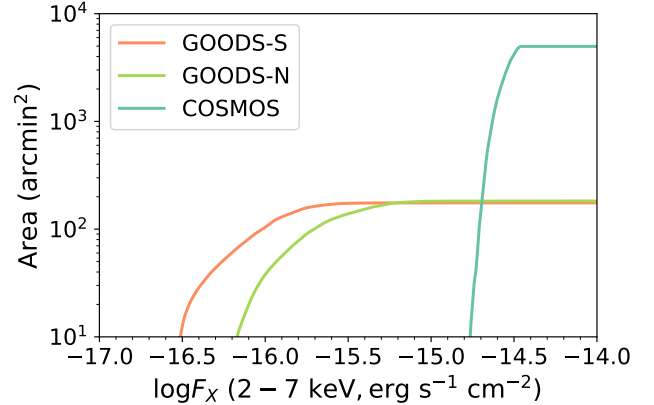


Figure 2. GOODS-S, GOODS-N, and COSMOS sky coverages as functions of hard-band (2–7 keV) X-ray flux. Different colors indicate different surveys. GOODS-S and GOODS-N are quite deep but cover small areas; COSMOS covers a larger area but is shallower than GOODS-S and GOODS-N.

2.1.2 COSMOS

We adopt the COSMOS2015 galaxy catalog for the COSMOS field (Laigle et al. 2016); the basic information for this field is summarized in Tab. 1. We only use sources within both the COSMOS and UltraVISTA regions, after removing the masked objects (1.38 deg²; see Fig. 1 and Tab. 7 in Laigle et al. 2016). The UltraVISTA region has deep NIR observations that are critical in SED fitting. The COSMOS2015 catalog includes sources detected in a χ^2 sum of $zYJHK_s$ images (see Szalay et al. 1999 for this detection technique). The 3σ limiting magnitude is $K_S \approx 24$. We note that this limiting magnitude is only a rough estimation of the depth of the K_S imaging data. The COSMOS2015 catalog is actually deeper than $K_S \approx 24$ due to the multiwavelength-based detection method used. In fact, $\approx 50\%$ of sources are fainter than $K_S \approx 24$. The multiwavelength photometric data in the COSMOS2015 catalog include 18 broad bands from GALEX NUV to *Spitzer*/IRAC, 12 medium optical bands, and 2 narrow optical bands (see Tab. 1 in Laigle et al. 2016).

The refined catalog consists of 520,778 galaxies with M_* and photometric-redshift measurements, among which 141,004 sources have $\log M_* > 9.5$. Compared with the spectroscopic redshifts available (Lilly et al. 2009), the photometric redshifts have a median uncertainty of 0.006 and an outlier fraction of 3%, thanks to the good coverage of the multiwavelength observations.¹ Fig. 1 (bottom) shows M_* vs. z for these sources. We also adopt the SED-based SFR measurements and perform star-forming vs. quiescent classifications as in §2.1.1.

Marchesi et al. (2016a) have matched these sources with the COSMOS-Legacy X-ray survey, which has 160 ks *Chan-*

¹ Laigle et al. (2016) derived M_* using the photometric redshifts. Thus, we do not adopt the spectroscopic redshifts for these objects even when these are available. Since their photometric redshifts agree well with the spectroscopic redshifts, the adoption of the former instead of the latter should not affect our conclusions materially.

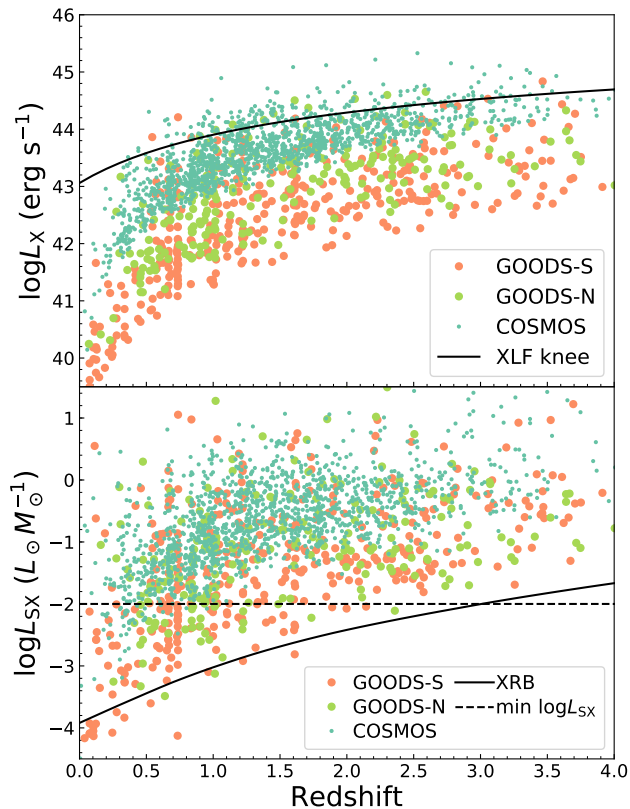


Figure 3. Top panel: L_X vs. z for the X-ray-detected sources in our sample. Different colors indicate sources from different surveys. The black solid curve indicates the XLF knee luminosity from Aird et al. (2015), who derived the knee luminosities for obscured and unobscured populations, respectively. Here, we adopt the values for the obscured AGNs, which are the majority population. The GOODS-S and GOODS-N sources are generally less luminous than COSMOS sources at a given redshift. Bottom panel: L_{SX} vs. z . The black solid curve represents the L_{SX} for X-ray binaries of galaxies on the star-forming main sequence (see §3.5.2). The black dashed horizontal line indicates our L_{SX} cut, i.e., $10^{-2} L_\odot M_\odot^{-1}$ (see 3.2.3).

dra effective exposure time (Civano et al. 2016). We utilize hard-band flux to derive L_X for hard-band detected sources as in §2.1.1. The sky coverage as a function of hard-band flux is shown in Fig. 2. COSMOS covers an area ≈ 30 times larger than GOODS-S/GOODS-N but is substantially shallower. The L_X and L_{SX} as functions of redshift are presented in Fig. 3. There are 1,448 X-ray AGNs with $\log L_{SX} > -2$ (see §3.2.3).

The ultra-deep fields of GOODS-S and GOODS-N and the medium-deep field COSMOS are complementary in sampling a wide range of L_X . At a given redshift, the most luminous COSMOS sources often have L_X a few times higher than the knee luminosity; the faintest GOODS sources have $L_X \approx 2$ decades below the knee luminosity. This wide range of sampled L_X typically includes $\gtrsim 70\%$ of the total L_X from the integral of the XLF. In this sense, our survey data sample contains most of cosmic accretion power.

2.1.3 Broad-Line AGNs

The photometric redshifts and M_\star in the survey catalogs (§2.1) are obtained from SED fitting with galaxy templates. This is appropriate for normal galaxies and non-BL AGNs where rest-frame UV to NIR SEDs are dominated by stellar light (see, e.g., Luo et al. 2010; Brandt & Alexander 2015; §2.2 of Yang et al. 2017). However, BL AGNs can be responsible for a large fraction of the total UV-to-NIR SED. When they are present, AGN components should be considered properly in SED fitting, and thus the redshift and M_\star measurements in the survey catalogs may not be reliable. There are 359 BL AGNs in our survey data identified from spectroscopic observations (GOODS-S: 22 sources from Silverman et al. 2010; GOODS-N: 15 sources from Barger et al. 2003; COSMOS: 322 sources from Marchesi et al. 2016a). These observations provide reliable spectroscopic redshifts for these BL AGNs.

Additional BL AGNs might be missed due to the lack of full spectroscopic coverage. Most of the missed BL AGNs should be in COSMOS due to its relatively large area. Now we estimate the number of possibly missed BL AGNs for COSMOS. For the ≈ 710 X-ray AGNs with high-quality spectra (Marchesi et al. 2016a), we find that BL AGNs are generally brighter and bluer than non-BL AGNs, and these two populations are separated in the color-magnitude diagram by $B - r = 0.8$ and $r = 24$ (observed AB magnitude; from Laigle et al. 2016). Applying this criterion ($B - r < 0.8$ and $r < 24$) to the ≈ 740 X-ray sources without high-quality spectra, we estimate that the missed BL AGN number in COSMOS is ≈ 70 , significantly smaller than the number of spectroscopically identified BL AGNs (322). We caution that there might be additional BL AGNs not satisfying the empirical criterion. However, those sources are faint ($r \geq 24$) and/or red ($B - r \geq 0.8$), and their AGN SED components are less likely to dominate over the host-galaxy components. Therefore, the missed BL AGNs in our sample should not affect our analyses significantly.

To obtain reliable M_\star for BL AGNs, we perform SED decomposition utilizing a minimum- χ^2 method implemented in CIGALE (Noll et al. 2009; Serra et al. 2011).² CIGALE can perform SED fitting for a source based on a set of photometric data at a given redshift, and output physical parameters like M_\star and SFR. We use the photometric data from the survey catalogs (§2.1) and redshifts from spectroscopic observations. The AGN model in Fritz et al. (2006) is implemented in CIGALE, and we follow the settings for the typical BL AGN template in Tab. 1 of Ciesla et al. (2015). We allow $frac_{AGN} = 0-1$ with a step of 0.05, where $frac_{AGN}$ is the AGN fractional contribution to the total IR luminosity. For galaxy components, we assume a Chabrier initial mass function (IMF; Chabrier 2003), which is also adopted to measure M_\star for galaxies in the survey data. We adopt a τ model of star formation history (SFH) and allow values for $\log(\tau/\text{yr})$ ranging from 8 to 10.5 with a step size of 0.5 dex. The stellar templates are from the model of Bruzual & Charlot (2003). We allow several possible values of metallicity ($Z = 0.0001, 0.0004, 0.004, 0.008, 0.02, 0.05$, where Z is the mass fraction of metals). We adopt the Calzetti extinction law (Calzetti et al. 2000) allowing $E(B - V)$ to vary

² <http://cigale.lam.fr/>

from 0.0–1.0 with a step of 0.1. CIGALE also includes nebular and dust emission (Noll et al. 2009; Draine & Li 2007). The above settings for galaxy SED is similar to those used to derive photometric redshifts and M_\star in the survey catalogs (Santini et al. 2015; Laigle et al. 2016; Barro et al. in prep.).

Fig. 4 displays the SED fitting for two typical BL AGNs. Although the AGN component can be dominant over the galaxy component at rest-frame UV-to-optical wavelengths, the galaxy component often contributes significantly to the total SED at NIR wavelengths ($\approx 1 \mu\text{m}$, rest-frame). This effect arises because emission from the AGN accretion disk and the torus are both relatively weak in the NIR, but starlight often peaks in the NIR (see, e.g., Fig. 1 of Calistro Rivera et al. 2016). The relatively high contrast of galaxy/AGN at NIR wavelengths ensures reliable M_\star measurements, since NIR flux is critical in assessing M_\star (e.g., Ciesla et al. 2015; Calistro Rivera et al. 2016).

We compare our updated M_\star values with those from the survey catalogs in Fig. 5. Here, we only compare BL AGNs having spectroscopic redshifts consistent with the redshifts from the catalogs [$|\Delta z|/(1+z_{\text{spec}}) < 0.15$; see Footnote 1]. The systematics between these two measurements are low with the median of $\Delta \log M_\star$ being 0.01 dex. The scatter (median of $|\Delta \log M_\star|$) is 0.26. The two measurements agree within 0.5 dex for the majority (73%) of sources. From Fig. 5, there is a group of sources with our M_\star values being significantly lower than the corresponding catalog M_\star values. These sources tend to be X-ray luminous ($\log L_X \gtrsim 44$; see Fig. 5), and their AGN SED components are comparable to or even dominant over their galaxy components in the NIR. Thus, the catalog measurements, which only utilize galaxy templates, significantly overestimate their M_\star . There are also some sources for which our M_\star measurements are ≈ 0.5 dex higher than the catalog measurements. The reason is likely that the catalog measurements underestimate the stellar age, resulting in small mass-to-light ratio. This is because when using galaxy templates only, the photometric data require young stellar age to account for the UV flux generated by the BL AGN.

Throughout the paper, for BL AGNs, we adopt the M_\star values derived from our AGN-galaxy SED decomposition rather than the catalog values.

We do not recalculate M_\star for non-BL AGNs. However, these sources might have strong AGN emission in the rest-frame mid-IR, contributing significantly to the observed SED, especially in the IRAC bands. To evaluate this effect, we compare our adopted M_\star values for non-BL AGNs in COSMOS with those from Suh et al. (2017), who included AGN components in SED fitting. The two sets of M_\star agree well: the offset and scatter are 0.08 dex and 0.11 dex, respectively. We thus conclude that the presence of non-BL AGNs does not bias our adopted M_\star measurements.

2.2 Stellar Mass Function and X-ray Luminosity Function

Our methodology also utilizes the SMF and XLF as inputs, which provide additional constraints to $P(L_{\text{SX}}|M_\star, z)$ besides the GOODS-S/GOODS-N/COSMOS data set (see §3.1.2), especially for luminous AGNs (see §3.1.2). We adopt the SMF from Behroozi et al. (2013). Their SMF is based on a

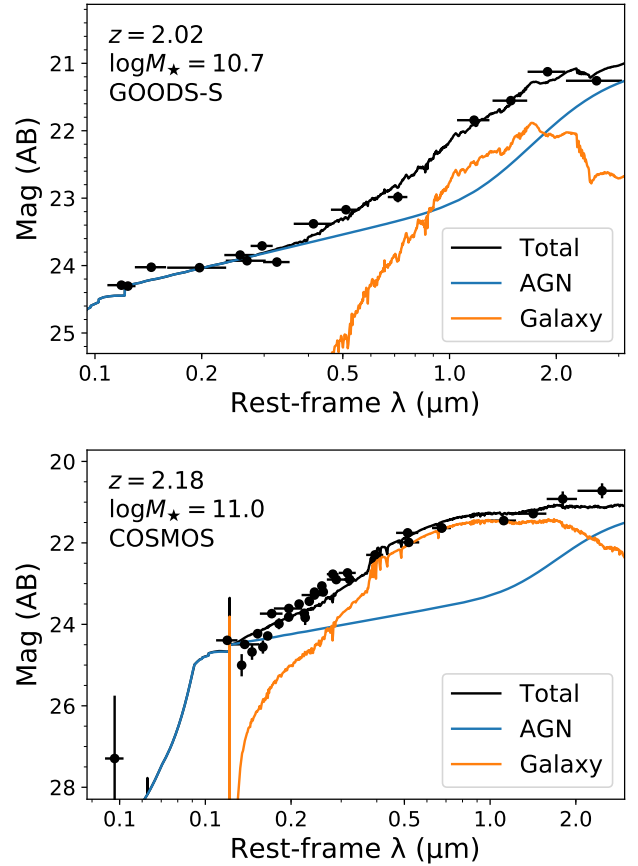


Figure 4. Two examples of our SED decomposition for BL AGNs. The black data points are observed photometry, and the black line indicates our best-fit SED model. The blue and orange lines represent the AGN and galaxy components, respectively. At rest-frame $\approx 1 \mu\text{m}$, the galaxy component often contributes significantly to the total SED.

galaxy evolution model that considers both star formation and mergers and is constrained by the observed SMF, specific SFRs ($\text{sSFR} = \text{SFR}/M_\star$), and ρ_{SFR} . The SMF model covers ranges of $\log M_\star = 7\text{--}12$ and $z = 0\text{--}8$. To evaluate the quality of this SMF, we compare it with the observational results of Davidzon et al. (2017) (see Fig. 3 in Behroozi et al. 2013 for comparison with some previous observations). Fig. 6 displays the results. The SMF from the Behroozi et al. (2013) model agrees well with the observed SMF values even at high redshift ($z \approx 4$).

We adopt the binned soft-band XLF values of Ueda et al. (2014) (see their Fig. 10). Fig. 7 compares the binned rest-frame 2–10 keV XLF derived from soft-band and hard-band observations.³ We choose the soft-band XLF instead of the hard-band XLF because the former extends to extremely high luminosity ($\log L_X \gtrsim 46$), largely due to the wide-field surveys of *ROSAT*. The soft-band XLF is already corrected for obscuration and is thus consistent with the hard-band XLF when available (see Fig. 7). In practice, adopting the

³ In Ueda et al. (2014), the hard-band data include various survey results above 2 keV (see their Tab. 1 for details).

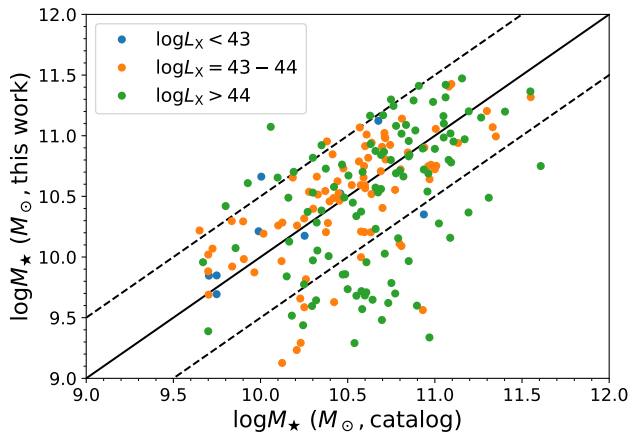


Figure 5. Comparison between the M_\star measurements from our SED fitting (with both BL AGN and galaxy templates) and those from the catalogs (with only galaxy templates; see §2.1). Different colors indicate AGNs in different L_X regimes. The black solid line indicates the 1:1 relation between the two M_\star measurements; the dashed lines indicate 0.5 dex offsets. A group of sources have our M_\star measurements significantly lower than the catalog values. These sources tend to be luminous AGNs with $\log L_X \gtrsim 44$.

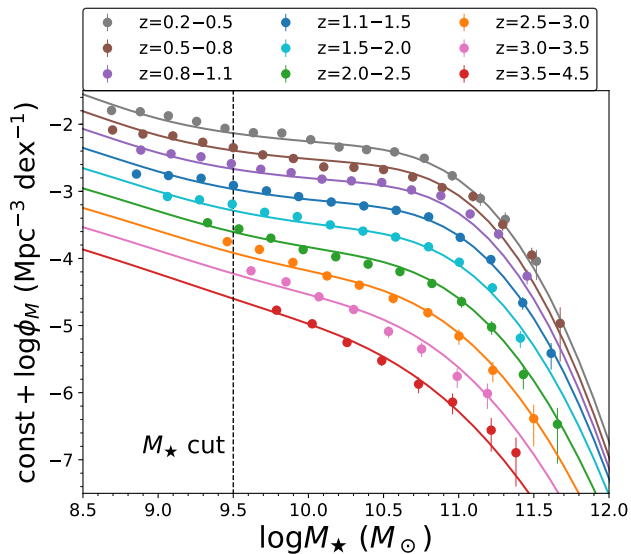


Figure 6. Stellar mass function. The solid curves indicate the SMF model from Behroozi et al. (2013). The data points are the observational results of Davidzon et al. (2017). Different colors indicate different redshifts. For display purposes only, the SMF (both the curve and data points) for a given redshift bin is shifted downward by 0.2 dex relative to the next lower redshift bin; the SMF for the lowest redshift bin is not shifted. The SMF model agrees well with the observations.

hard-band XLF would only have minor effects on our results (§3.4). We have also compared the XLFs from Ueda et al. (2014) with those from Aird et al. (2015), and found they agree well. Since Ueda et al. (2014) extend to higher L_X than Aird et al. (2015), we adopt the XLF results from Ueda et al. (2014). The XLF data points in Ueda et al. (2014) are

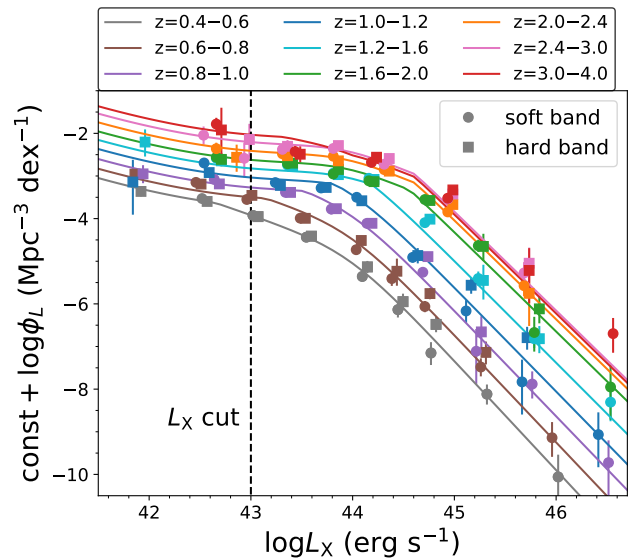


Figure 7. X-ray luminosity function. The circles and squares indicate the binned XLF values derived from the soft band and hard band, respectively, in Ueda et al. (2014). The hard-band data are shifted slightly toward the right for display purposes only. The solid curves are the best-fit XLF model in Ueda et al. (2014). The soft-band XLF agrees well with the hard-band XLF. Different colors indicate different redshifts. For display purposes only, the XLF (both the curve and data points) for a given redshift bin is shifted upward by 0.3 dex relative to the next lower redshift bin; the XLF for the lowest redshift bin is not shifted. The vertical dashed solid line indicates our L_X cut ($\log L_X = 43$) for the XLF.

derived from all X-ray detected sources with $\log L_X \gtrsim 42$, and thus components of XRBs might become important at the low-luminosity end. To avoid this XRB contamination, we only adopt the XLF at $\log L_X > 43$. Also, we do not probe the low- L_{SX} regime ($\log L_{\text{SX}} < -2$; see §3.2.3) that could significantly contribute to the XLF at $\log L_X < 43$. For example, at $\log L_X = 42-42.5$, 32% of the X-ray sources in our sample have $\log L_{\text{SX}} < -2$. At $\log L_X < 43$, our $P(L_{\text{SX}}|M_\star, z)$ are constrained by the survey data (see §2.1) which have ≈ 420 X-ray AGNs with $\log L_X < 43$.

2.3 Bolometric Correction

To obtain $\overline{\text{BHAR}}$ from the $P(L_{\text{SX}}|M_\star, z)$, we require a bolometric correction ($k_{\text{bol}} = L_{\text{bol}}/L_X$) which is a function of AGN luminosity (e.g., Steffen et al. 2006; Hopkins et al. 2007; Lusso et al. 2012, see §3.4 for $\overline{\text{BHAR}}$ calculation). Our k_{bol} is based on the results of Lusso et al. (2012), which are derived from the multiwavelength observations of X-ray selected AGNs. We did not adopt the k_{bol} from Hopkins et al. (2007), because they included the dust-reprocessed IR emission that is not directly produced by AGN accretion power. This inclusion results in a fraction of the accretion-powered radiation being accounted for twice. Thus, their k_{bol} serves as an empirical bolometric correction but is an overestimation for our purpose, i.e., to infer the accretion power of the SMBH.

Lusso et al. (2012) modeled k_{bol} as polynomials of AGN L_{bol} for BL ($k_{\text{bol, BL}}$) and non-BL AGNs ($k_{\text{bol, nBL}}$), respec-

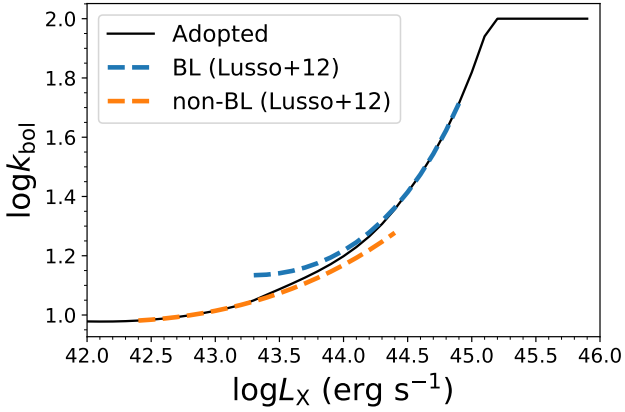


Figure 8. Bolometric correction as a function of X-ray luminosity. The black solid line indicates the k_{bol} adopted in this work. The blue and orange dashed lines indicate k_{bol} for BL and non-BL AGNs, respectively, in [Lusso et al. \(2012\)](#). k_{bol} generally increases toward high L_X .

tively (see their Tab. 2). We present their $k_{\text{bol,BL}}$ and $k_{\text{bol,nBL}}$ as a function of L_X in Fig. 8 (dashed curves). Both $k_{\text{bol,BL}}$ and $k_{\text{bol,nBL}}$ are positively dependent on L_X . The differences between $k_{\text{bol,BL}}$ and $k_{\text{bol,nBL}}$ are small ($\lesssim 0.1$ dex), consistent with the standard unified AGN model. The BL AGNs are generally more luminous than the non-BL AGNs in [Lusso et al. \(2012\)](#). Denoting the overlapping L_X range of the BL and non-BL as $L_{X,1} - L_{X,2}$, we adopt $k_{\text{bol,nBL}}$ if $L_X < L_{X,1}$ and $k_{\text{bol,BL}}$ if $L_X > L_{X,2}$. For $L_{X,1} \leq L_X \leq L_{X,2}$, we adopt k_{bol} as

$$k_{\text{bol}} = k_{\text{bol,BL}} \frac{L_X - L_{X,1}}{L_{X,2} - L_{X,1}} + k_{\text{bol,nBL}} \frac{L_{X,2} - L_X}{L_{X,2} - L_{X,1}}. \quad (1)$$

This linear interpolation produces a smooth k_{bol} as a function of L_X (see Fig. 8). $k_{\text{bol,BL}}$ diverges quickly toward high L_X due to the polynomial functional form of k_{bol} that [Lusso et al. \(2012\)](#) assumed. To avoid this divergence, we set an upper limit of 100 for the adopted k_{bol} , which is about the maximum value of k_{bol} reported in the literature (e.g., [Marconi et al. 2004](#); [Hopkins et al. 2007](#)).

Some studies suggest that k_{bol} might also be related to λ_{Edd} (e.g., [Vasudevan & Fabian 2007](#); but also see [Shemmer et al. 2008](#)). While it is still under investigation whether k_{bol} is more fundamentally related to AGN luminosity or λ_{Edd} , we adopt the $k_{\text{bol}}-L_X$ relation because we are not able to obtain λ_{Edd} accurately. We discuss the effects of a $k_{\text{bol}}-\lambda_{\text{Edd}}$ relation in §3.4.1.

3 DATA ANALYSES

We derive $\overline{\text{BHAR}}(M_\star, z)$ from $P(L_{\text{SX}}|M_\star, z)$ (§3.4), which is constrained utilizing maximum-likelihood fitting (§3.3). The fitting requires likelihood functions, and our likelihood functions are based on the survey data (§3.1.1) as well as the SMF and XLF (§3.1.2). The survey data mostly constrain $P(L_{\text{SX}}|M_\star, z)$ for low-to-moderate luminosity AGNs, while the SMF and XLF constrain $P(L_{\text{SX}}|M_\star, z)$ for luminous AGNs.

3.1 Likelihood Functions

3.1.1 The Likelihood Function of Survey Data

With the survey data providing L_X , M_\star , and z for individual sources (§2), we can derive the corresponding likelihood function, which quantifies how well the input $P(L_{\text{SX}}|M_\star, z)$ model matches the survey data. The methodology is detailed in §6.1 of [Aird et al. \(2012\)](#); below we briefly summarize this technique.

For each survey in §2.1, we denote the number of detected X-ray AGNs as N_{AGN} , where we only consider X-ray sources with $\log L_{\text{SX}} > -2$ as AGNs (see §3.2.3). The log-likelihood function for this survey can be derived from the unbinned Poisson probability (e.g., [Loredo 2004](#)) as

$$\ln L = -N_{\text{mdl}} + \sum_{i=1}^{N_{\text{AGN}}} \ln P(L_{\text{SX},i}|M_{\star,i}, z_i), \quad (2)$$

where N_{mdl} is the expected number of X-ray detected AGNs from the input $P(L_{\text{SX}}|M_\star, z)$ model. In the survey area, there are N_{gal} galaxies within the redshift range, each with M_\star and redshift measurements. The quantity N_{mdl} can be calculated as

$$\begin{aligned} N_{\text{mdl}} &= \sum_{i=1}^{N_{\text{gal}}} \int_{-2}^{\infty} P(L_{\text{SX}}|M_{\star,i}, z_i) p_{\text{det}}(L_X, z_i) d \log L_{\text{SX}} \\ &= \sum_{i=1}^{N_{\text{gal}}} \int_{-2}^{\infty} P(L_{\text{SX}}|M_{\star,i}, z_i) p_{\text{det}}(L_{\text{SX}} M_{\star,i}, z_i) d \log L_{\text{SX}}, \end{aligned} \quad (3)$$

where p_{det} , as a function of L_X and z , is the correction factor for survey sensitivity. The integral lower limit (-2) is the lowest L_{SX} probed in this work, and we discuss the effects of this L_{SX} cut in §3.2.3. $p_{\text{det}}(L_X, z)$ is defined as

$$p_{\text{det}}(L_X, z) = \frac{A[f(L_X, z)]}{A_{\text{tot}}}, \quad (4)$$

where $f(L_X, z)$ is the expected X-ray flux in the detection band for a source with L_X at redshift z ; $A[f(L_X, z)]$ is the sky coverage of the survey sensitive to the flux $f(L_X, z)$ (Fig. 2); A_{tot} is the total survey area.

We calculate the log-likelihood for each survey (GOODS-S, GOODS-N, and COSMOS; see §2.1) independently according to Eq. 2, and combine them as

$$\ln L_{\text{surv}} = \ln L_{\text{GOODS-S}} + \ln L_{\text{GOODS-N}} + \ln L_{\text{COSMOS}}. \quad (5)$$

Since our data only include 0.05–1.4 deg² surveys, most of our X-ray selected sources are low-to-moderate luminosity AGNs ($\log L_X \lesssim 44.5$; see Fig. 3), and the number of luminous AGNs is limited. However, this small-area effect does not introduce biases for these luminous AGNs, because the sizes of the survey areas are already properly considered in the likelihood function through the term “ N_{mdl} ” (see Eq. 3). Moreover, $P(L_{\text{SX}}|M_\star, z)$ for luminous AGNs is constrained by our SMF-XLF methodology in §3.1.2.

3.1.2 The Likelihood Function of SMF and XLF

Besides the constraints from the survey data, we can also constrain $P(L_{\text{SX}}|M_\star, z)$ utilizing the SMF and XLF. By definition, the SMF provides the comoving number density of galaxies at given M_\star and z . Thus, we can convolve the SMF

with $P(L_{\text{SX}}|M_\star, z)$ at a given redshift to obtain the comoving number density of AGNs at given L_X and z (i.e., the XLF),

$$\begin{aligned}\phi_L(L_X|z) &= \int_{9.5}^{12} P(L_{\text{SX}}|M_\star, z)\phi_M(M_\star|z)d\log M_\star \\ &= \int_{9.5}^{12} P(L_X/M_\star|M_\star, z)\phi_M(M_\star|z)d\log M_\star,\end{aligned}\quad (6)$$

where ϕ_L and ϕ_M are the XLF and SMF, respectively. Both ϕ_L and ϕ_M are in units of $\text{Mpc}^{-3} \text{dex}^{-1}$. The integral range ($\log M_\star = 9.5\text{--}12$) corresponds to the M_\star regime probed in our analyses, and we discuss the effects of this M_\star cut in §3.2.2.

To evaluate quantitatively how well a model $P(L_{\text{SX}}|M_\star, z)$ meets the constraints from the SMF and XLF (§2.2), we compare N_{mdl} and the observed numbers of X-ray sources (N_{obs}) for each ϕ_L bin in Ueda et al. (2014). For any given model of $P(L_{\text{SX}}|M_\star, z)$, we can obtain the corresponding model XLF ($\phi_{L,\text{mdl}}$) via Eq. 6. We can convert $\phi_{L,\text{mdl}}$ to N_{mdl} as

$$N_{\text{mdl}} = \phi_{L,\text{mdl}} \frac{N_{\text{obs}}}{\phi_{L,\text{obs}}}, \quad (7)$$

where $N_{\text{obs}}/\phi_{L,\text{obs}}$ is the conversion factor between the number of sampled X-ray sources and the XLF in Ueda et al. (2014). $N_{\text{obs}}/\phi_{L,\text{obs}}$ considers many factors such as X-ray survey area and sensitivity and is provided by Y. Ueda (2017, private communication). We can then obtain the log-likelihood function for the SMF and XLF as

$$\ln L_{\text{XLF}} = \sum_{i=1}^n \ln P(N_{\text{obs},i}|\lambda = N_{\text{mdl},i}), \quad (8)$$

where n is the total number of L_X and redshift bins available for the XLF, and $P(N_{\text{obs},i}|\lambda = N_{\text{mdl},i})$ is the Poisson probability of $N_{\text{obs},i}$ events for the rate parameter $\lambda = N_{\text{mdl},i}$.

Since we apply an L_X cut to the XLF ($\log L_X > 43$; see §2.2), the SMF-XLF method does not constrain $P(L_{\text{SX}}|M_\star, z)$ for low-luminosity AGNs. In fact, this method is also not very effective when assessing moderate-luminosity AGNs with $43 < \log L_X \lesssim 44$. For example, for an AGN with $\log L_X \approx 43.5$, its host galaxy can be either a moderate- M_\star galaxy with relatively high L_{SX} (e.g., $\log M_\star \approx 10$ and $\log L_{\text{SX}} \approx 0$) or a high- M_\star galaxy with low L_{SX} (e.g., $\log M_\star \approx 11$ and $\log L_{\text{SX}} \approx -1$). The SMF-XLF method cannot determine which case is more probable, although it does require that the sum of the contributions from all galaxies must match the AGN number density. However, this degeneracy is weak in the high- L_X regime. For example, for an AGN with $\log L_X \approx 45$, its host galaxy is likely massive ($\log M_\star \gtrsim 11$) with moderate-to-high L_{SX} ($-0.5 \lesssim \log L_{\text{SX}} \lesssim 0.5$); otherwise, the corresponding L_{SX} would be too high and far beyond the high- L_{SX} cutoff ($\log L_{\text{SX}} \approx 0$; see, e.g., Bongiorno et al. 2016; Aird et al. 2017a; Georgakakis et al. 2017). This is the reason why the SMF-XLF method is most effective for luminous AGNs.

3.2 Cuts in Parameter Space

3.2.1 Redshift Cuts

We limit our study to the redshift range of $z = 0.4\text{--}4$. The primary reason for this is that we have a limited number of X-ray AGNs outside this redshift range. Quantitatively, the

number of AGNs with $z < 0.4$ or $z > 4$ is 89 which accounts for only $\approx 5\%$ of the whole AGN sample.

3.2.2 M_\star Cuts

In this work, we only study galaxies having $\log M_\star = 9.5\text{--}12$. The reason for the lower cut of M_\star is that X-ray AGNs are rarely detected in low- M_\star galaxies (see Fig. 1); in our sample (§2.1), only $\approx 5\%$ of X-ray AGNs are detected with $\log M_\star < 9.5$. The low detection rate of X-ray AGNs for the low- M_\star systems makes it challenging to constrain effectively $P(L_{\text{SX}}|M_\star, z)$ for these sources. We investigate galaxies with M_\star up to $\log M_\star = 12$. In our sample, there are ≈ 190 galaxies with $\log M_\star = 11.5\text{--}12$ but only 7 galaxies above $\log M_\star = 12$.

These M_\star cuts have little effect on our methods in §3.1.2, because the XLF is dominated by AGNs hosted in galaxies with $\log M_\star = 9.5\text{--}12$. At $\log L_X = 43\text{--}43.5$ (the lowest-luminosity bin we adopt for the XLF; see §2.2), almost all (98%) AGN-host galaxies have $\log M_\star = 9.5\text{--}12$ in our sample, and the fraction is even larger toward higher luminosities.

3.2.3 L_{SX} Cut

We cannot probe low L_{SX} values at high redshift due to survey sensitivity. For example, we only have two sources with $\log L_{\text{SX}} < -2$ at $z > 2$. Also, at low L_{SX} , it is difficult to disentangle X-ray emission from AGNs and XRBs (see §3.5.2). We thus limit our investigation to $\log L_{\text{SX}} \geq -2$.

This L_{SX} cut has little effect on our SMF-XLF method (§3.1.2), since galaxies with $\log L_{\text{SX}} < -2$ have almost no contribution to the XLF above $\log L_X = 43$ (the lowest L_X we adopt for the XLF; see §2.2). For example, among the $\approx 1,500$ AGNs with $\log L_X \geq 43$ in our sample, only one source has $\log L_{\text{SX}} < -2$.

Now we demonstrate that SMBH accretion below $\log L_{\text{SX}} = -2$ does not contribute significantly to the growth of SMBHs over cosmic history. The Eddington ratio is defined as

$$\begin{aligned}\lambda_{\text{Edd}} &= \frac{L_{\text{bol}}}{L_{\text{Edd}}} \\ &= \frac{\epsilon \text{BHAR} c^2}{1.3 \times 10^{38} \text{ erg s}^{-1} M_{\text{BH}} M_\odot^{-1}} \\ &= \frac{M_\odot c^2}{1.3 \times 10^{39} \text{ erg s}^{-1}} \frac{\text{BHAR} \epsilon_{0.1}}{M_{\text{BH}}} \\ &= 0.044 \text{ Gyr} \frac{\text{BHAR} \epsilon_{0.1}}{M_{\text{BH}}},\end{aligned}\quad (9)$$

where c is the speed of light, ϵ is radiation efficiency, and $\epsilon_{0.1} = \epsilon/0.1$. λ_{Edd} can also be related to L_{SX} as

$$\begin{aligned}\lambda_{\text{Edd}} &= \frac{L_{\text{bol}}}{L_{\text{Edd}}} \\ &= \frac{k_{\text{bol}} L_X}{3.2 \times 10^4 L_\odot M_{\text{BH}} M_\odot^{-1}} \\ &= \frac{10 \times 5000}{3.2 \times 10^4} \frac{L_X L_\odot^{-1}}{M_\star M_\odot^{-1}} \frac{k_{\text{bol}}}{10} \frac{M_\star}{5000 M_{\text{BH}}} \\ &= 1.6 L_{\text{SX}} k_{10} m_5,\end{aligned}\quad (10)$$

where $k_{10} = k_{\text{bol}}/10$ and $m_5 = M_\star/(5000 M_{\text{BH}})$. From Eqs. 9

and 10, we can obtain the e -folding timescale of SMBH growth as

$$t_e = \frac{M_{\text{BH}}}{\text{BHAR}} = 0.028 \text{ Gyr} \frac{\epsilon_{0.1}}{L_{\text{SX}} k_{10} m_5}. \quad (11)$$

$\log L_{\text{SX}} < -2$ corresponds to $\log L_X \lesssim 43.5$ with $k_{10} \approx 1$ (see Fig. 8). Assuming the average L_{SX} for this low- L_{SX} ($\log L_{\text{SX}} < -2$) accretion is $\approx 10^{-2.5}$ and $\epsilon_{0.1} \approx 1$, then $t_e \approx 9m_5^{-1}$ Gyr. From our results in Sec. 4.3, m_5 ranges from ≈ 0.1 to 1 up to at least $z \approx 2$. Thus, the growth time for low- L_{SX} accretion should be $t_e \approx 9\text{--}90$ Gyr comparable to or longer than the Hubble time. Therefore, the accretion with $\log L_{\text{SX}} < -2$ is unlikely important in our overall understanding of SMBH growth.

The above argument assumes $\epsilon \approx 0.1$, which is typical for a cold accretion disk (e.g., Shakura & Sunyaev 1973; Agol & Krolik 2000). For hot accretion flows, ϵ can be much lower ($\epsilon \lesssim 0.01$). However, such low ϵ only arises when the accretion rate is low, i.e.,

$$\frac{0.1\text{BHAR}c^2}{L_{\text{Edd}}} \lesssim 10^{-3}, \quad (12)$$

(see Fig. 2 of Yuan & Narayan 2014). Under this condition, the SMBH growth timescale is

$$\begin{aligned} t_e &= \frac{M_{\text{BH}}}{\text{BHAR}} \\ &= \frac{L_{\text{Edd}}}{1.3 \times 10^{38} \text{BHAR erg s}^{-1} M_{\odot}^{-1}} \\ &= \frac{M_{\odot} c^2}{1.3 \times 10^{39} \text{ erg s}^{-1} 0.1\text{BHAR}c^2} \\ &\gtrsim \frac{M_{\odot} c^2}{1.3 \times 10^{39} \text{ erg s}^{-1}} \times 10^3 \\ &\approx 44 \text{ Gyr}, \end{aligned} \quad (13)$$

which is also longer than Hubble time. Therefore, low- ϵ accretion states should not contribute significantly to the overall SMBH growth across cosmic history.

Our argument above shows that low- L_{SX} accretion cannot increase M_{BH} effectively over cosmic history. However, low- L_{SX} accretion might still contribute more significantly to $\overline{\text{BHAR}}$ than high- L_{SX} accretion in specific limited ranges of redshift and M_{\star} . In such regimes, our $\overline{\text{BHAR}}$ calculation, which does not account for low- L_{SX} accretion, will be inaccurate. We discuss this possibility in §3.5.4.

3.3 Maximum-Likelihood Fitting of $P(L_{\text{SX}}|M_{\star}, z)$

The likelihood functions from survey data and the SMF-XLF data are the most effective in constraining $P(L_{\text{SX}}|M_{\star}, z)$ for AGNs in different L_X regimes (see §3.1). Thus, they need to be combined to identify the best model for $P(L_{\text{SX}}|M_{\star}, z)$. We obtain the final log-likelihood function as

$$\ln L = \ln L_{\text{surv}} + \ln L_{\text{XLF}}, \quad (14)$$

where $\ln L_{\text{surv}}$ and $\ln L_{\text{XLF}}$ are the log-likelihood functions in Eqs. 5 and 8, respectively. For a given model, we search for best-fit model parameters via maximum-likelihood fitting with IMINUIT v1.2.⁴

⁴ See <https://pypi.python.org/pypi/iminuit> for IMINUIT.

Following Bongiorno et al. (2016), we model $P(L_{\text{SX}}|M_{\star}, z)$ as a smoothed double power law. We do not adopt a single power-law model or a Schechter model (Schechter 1976) of $P(L_{\text{SX}}|M_{\star}, z)$. A single power law would lead to an unphysical divergent $\overline{L_X}$ (see §1). A Schechter model results in an exponential decline toward high L_X in the predicted XLF (see Eq. 6), inconsistent with the observed power-law decline (e.g., Ueda et al. 2014; Aird et al. 2015). However, a smoothed double power law can produce a power-law decline in the XLF. The smoothed double power law at given M_{\star} and z is written as

$$P(L_{\text{SX}}|M_{\star}, z) = A \left[\left(\frac{L_{\text{SX}}}{L_c} \right)^{\gamma_1} + \left(\frac{L_{\text{SX}}}{L_c} \right)^{\gamma_2} \right]^{-1}. \quad (15)$$

We define $\gamma_1 \leq \gamma_2$, and thus they are the slopes in the low and high L_{SX} regimes, respectively. All of $\log A$, $\log L_c$, γ_1 , and γ_2 are modeled in the general form of polynomial functions of $\log M_{\star}$ and $\log(1+z)$, i.e.,

$$\begin{aligned} X &= X_0 + \alpha_0^X \log(1+z) + \alpha_1^X \log M_{10} \\ &\quad + \beta_0^X [\log(1+z)]^2 + \beta_1^X \log(1+z) \log M_{10} + \beta_2^X (\log M_{10})^2 \\ &\quad + \dots \end{aligned} \quad (16)$$

where $M_{10} = M_{\star}/10^{10} M_{\odot}$, and X indicates $\log A$, $\log L_c$, γ_1 , or γ_2 .

To determine the highest order of polynomial necessary for each X , we perform a detailed model selection presented in Appendix A. We find that $\log A$, $\log L_c$, and γ_2 are consistent with 2nd-order, 2nd-order, and 1st-order polynomials, respectively; γ_1 is consistent with a constant value (0th-order polynomial). The best-fit parameter values and their errors are listed in Tab. 2; these errors are estimated from MCMC sampling (see Appendix A). Our conclusions (§4) are robust under $> 3\sigma$ confidence levels. The fitting quality and comparison with previous work are presented in Appendix B.

We are aware that there is an issue of “double-counting” when combining the likelihood functions in Eq. 14, since there are some AGNs being included in both survey and XLF data. This could lead to underestimation of our model uncertainties. However, we expect that this issue only has minor effects on our results. For COSMOS AGNs, this issue does not exist because the XLF measurements do not include them (see Tab. 1 of Ueda et al. 2014). For CDF-S and CDF-N, only AGNs above $\log L_X = 43$ (our L_X cut for XLF; see §2.2) are counted doubly, and these objects account for only $\approx 50\%$ of the whole AGN population in these two fields.

3.4 The Results for $\overline{\text{BHAR}}(M_{\star}, z)$

The main goal of this paper is to characterize the overall SMBH growth for the majority galaxy population at $z = 0.4\text{--}4$. Therefore, we derive the $\overline{\text{BHAR}}$ for all galaxies, including both star-forming and quiescent populations, in §3.4.1. We also study the $\overline{\text{BHAR}}$ for star-forming galaxies in §3.4.2. We do not investigate the $\overline{\text{BHAR}}$ for quiescent galaxies, as explained in §3.4.3.

3.4.1 All Galaxies

Due to the existence of strong AGN variability, ensemble-averaged $\overline{\text{BHAR}}$ is often adopted as an approximation of

Table 2. Best-Fit Model Parameters and 1σ Errors

	X_0	α_0^X	α_1^X	β_0^X	β_1^X	β_2^X
$\log A$	$-2.68^{+0.18}_{-0.19}$	$0.81^{+0.68}_{-0.85}$	$1.33^{+0.26}_{-0.20}$	$-0.20^{+1.04}_{-0.90}$	$1.00^{+0.43}_{-0.46}$	$-0.76^{+0.09}_{-0.11}$
$\log L_c$	$-0.57^{+0.19}_{-0.21}$	$4.66^{+0.90}_{-0.62}$	$-1.61^{+0.30}_{-0.39}$	$-4.24^{+0.82}_{-1.07}$	$0.90^{+0.62}_{-0.57}$	$0.46^{+0.16}_{-0.12}$
γ_1	$0.43^{+0.04}_{-0.02}$	–	–	–	–	–
γ_2	$2.45^{+0.27}_{-0.16}$	$-0.88^{+0.72}_{-0.52}$	$0.56^{+0.19}_{-0.36}$	–	–	–

NOTE. — The parameters are the polynomial coefficients in Eq. 16. The symbol “–” indicates the corresponding parameter is not required, and hence fixed to zero in our modeling (see Appendix A).

long-term average BHAR (see §1). From our derived L_{SX} distribution, we can obtain this $\overline{\text{BHAR}}$ as a function of M_\star and redshift, i.e.,

$$\begin{aligned} \overline{\text{BHAR}}(M_\star, z) &= \int_{-2}^{\infty} P(L_{SX}|M_\star, z) \frac{(1-\epsilon)k_{\text{bol}}(L_X)L_X}{\epsilon c^2} d \log L_{SX} \\ &= \int_{-2}^{\infty} P(L_{SX}|M_\star, z) \frac{(1-\epsilon)k_{\text{bol}}(M_\star L_{SX})M_\star L_{SX}}{\epsilon c^2} d \log L_{SX}. \end{aligned} \quad (17)$$

We use the $k_{\text{bol}}(L_X)$ function presented in §2.3. Although theoretical studies suggest that ϵ depends on factors like SMBH spin and the state of accretion flow (e.g., Shakura & Sunyaev 1973; Agol & Krolik 2000; Yuan & Narayan 2014), it is not feasible to determine ϵ accurately for individual AGNs from observations. The adopted $\epsilon = 0.1$ is likely a typical value for the overall AGN population (e.g., Marconi et al. 2004; Davis & Laor 2011), and has been widely adopted in previous work (e.g., Mullaney et al. 2012; Chen et al. 2013; Yang et al. 2017). We caution that there might be uncertainties up to a factor of a few for this typical ϵ .

The results are displayed in Fig. 9. As explained in Appendix B and §3.5.5, the model uncertainties at $z \lesssim 1$ and $\log M_\star \gtrsim 11.5$ might be underestimated due to limited AGN sample sizes and k_{bol} uncertainties. Therefore, we mark $\overline{\text{BHAR}}$ in these ranges as dotted curves in Fig. 9. Our derived $\overline{\text{BHAR}}(M_\star, z)$ shows that, at a given redshift, $\overline{\text{BHAR}}$ generally increases toward high M_\star , although the M_\star dependence is weaker toward the local universe. This positive $\overline{\text{BHAR}}-M_\star$ relation is also reported by Yang et al. (2017). Their data are consistent with a linear $\overline{\text{BHAR}}-M_\star$ (in logarithmic space) relation with a slope of unity for sources at $z = 0.5-2$ (the dashed line in Fig. 9).

BHAR has stronger redshift evolution at higher M_\star . For instance, for $\log M_\star = 9.5$, $\overline{\text{BHAR}}$ at $z = 4$ is 0.7 ± 0.4 dex higher than at $z = 0.5$; for $\log M_\star = 11.5$, $\overline{\text{BHAR}}$ rises by 3.0 ± 0.3 dex from $z = 0.5$ to $z = 4$. This strong redshift dependence for massive galaxies is also found by recent works (e.g., Aird et al. 2017a; Georgakakis et al. 2017). Yang et al. (2017) compared the $\overline{\text{BHAR}}-M_\star$ relations for two broad redshift bins, $z = 0.5-1.3$ and $z = 1.3-2.0$, but did not find significant differences, possibly due to the limited sample size of the GOODS-S field in their study (§2.1.1). Their relatively small sample lacks luminous AGNs (see Fig. 3), and could lead to a generally underestimated BHAR. This underestimation should be stronger at higher redshifts, where luminous AGNs contribute more significantly to ρ_{BHAR} than less-luminous AGNs (e.g., Ueda et al. 2014). In this work,

we included the COSMOS field that probes more luminous AGNs than GOODS-S at a given redshift (§2.1.2). Also, our methodology based on SMF and XLF provides further constraints on the luminous AGNs’ contribution to $\overline{\text{BHAR}}$ (see §3.1.2).

Since $\overline{\text{BHAR}}$ has a positive dependence on M_\star in general, we expect more massive galaxies to have higher M_{BH} in the local universe. However, the final M_{BH} not only depends on M_\star at $z = 0$, but also on the stellar mass history [$M_\star(z)$].⁵ Galaxy evolution is complex, e.g., high- M_\star galaxies tend to form earlier in cosmic history than low- M_\star galaxies (“galaxy downsizing”; e.g., Cowie et al. 1996). In §4.3 and §4.4, we consider all these effects and predict typical $M_{\text{BH}}-M_\star$ relations at different redshifts.

3.4.2 Star-forming Galaxies

The $\overline{\text{BHAR}}-M_\star$ slope in §3.4.1 becomes shallower toward low redshift. This could be due to the fact that the quiescent galaxy population becomes increasingly significant at low redshifts in massive galaxies (e.g., Brammer et al. 2011; Tomczak et al. 2014), and that quiescent galaxies generally have weaker AGN activity compared to star-forming galaxies (e.g., Rosario et al. 2013b; Aird et al. 2017a; Wang et al. 2017). To test this scenario, we derive $\overline{\text{BHAR}}(M_\star, z)$ for star-forming galaxies. We only use the survey-data constraints (§3.1.1), as the SMF-XLF constraints (§3.1.2) are for the whole galaxy population rather than the star-forming subset.

We select star-forming galaxies using the classifications in §2.1, which are not applied to BL AGNs. We now discuss the star-forming/quiescent types for BL AGNs. The star-forming population is dominant over the quiescent population for $\log M_\star \lesssim 10.5$ or $z \gtrsim 2$. Therefore, we assign a BL AGN to be star-forming if it satisfies $\log M_\star \lesssim 10.5$ or $z \gtrsim 2$, and this accounts for the majority population ($\approx 70\%$) of the BL AGNs. For the other 30% of BL AGNs, we include them in our $\overline{\text{BHAR}}(M_\star, z)$ derivation considering two extreme scenarios. The first scenario is that these 30% of BL AGNs are all star-forming (e.g., Zhang et al. 2016); the second is that they are all quiescent. The resulting $\overline{\text{BHAR}}(M_\star, z)$ for

⁵ For example, consider two galaxies (dubbed “A” and “B”) that both have $\log M_\star(z = 0) = 11.5$, but A forms earlier than B. Assume at $z = 2$, A and B have $\log M_\star = 11$ and 10, respectively. Then A has much higher $\overline{\text{BHAR}}$ than B at $z = 2$, according to Fig. 9. Therefore, the final $M_{\text{BH}}(z = 0)$ of A will be higher than that of B.

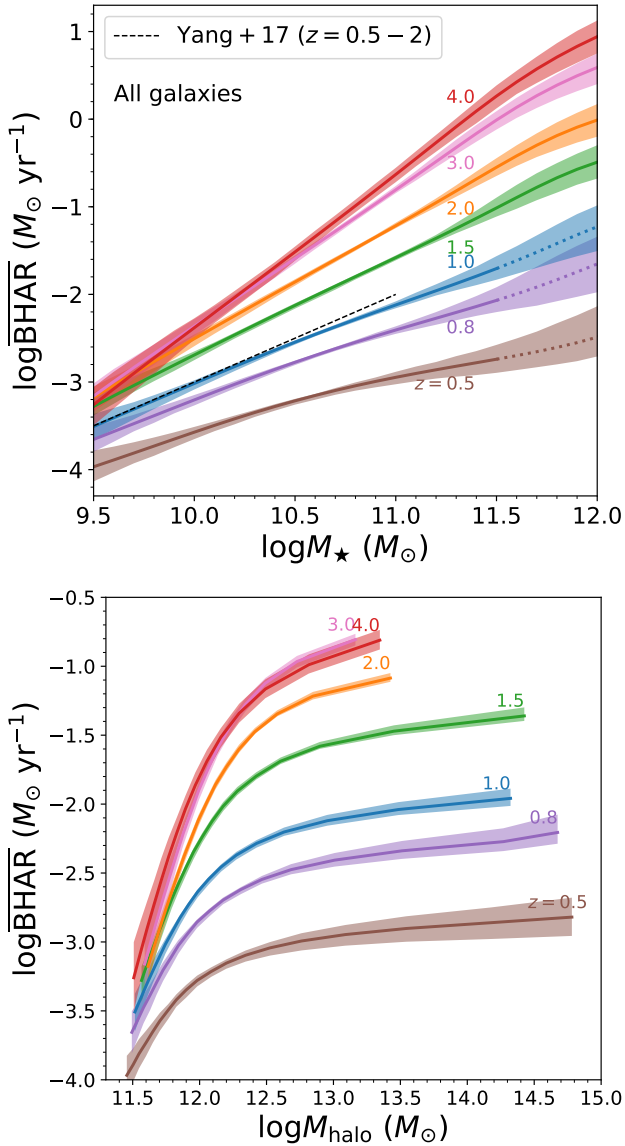


Figure 9. Top panel: $\overline{\text{BHAR}}$ for all galaxies, derived from our best-fit $P(L_{\text{SX}}|M_{\star}, z)$ model, as a function of M_{\star} and redshift. Different colors indicate different redshifts as labeled. The shaded regions indicate 1σ uncertainties derived from our MCMC sampling (see Appendix A). The dotted curves indicate the redshift and M_{\star} regimes ($z \lesssim 1$ and $\log M_{\star} \gtrsim 11.5$) where $\overline{\text{BHAR}}$ might have larger uncertainties than estimated (see §3.5.5 and Appendix B). The dashed black line indicates the best-fit relation from Eq. 6 of Yang et al. (2017) based on GOODS-S sources at $z = 0.5\text{--}2.0$. Bottom panel: Same format as the top panel but for $\overline{\text{BHAR}}$ vs. M_{halo} . $\overline{\text{BHAR}}$ is positively dependent on M_{halo} for $\log M_{\text{halo}} \lesssim 12\text{--}13$, but the dependence becomes much weaker toward higher M_{halo} . There are no corresponding dotted curves (large $\overline{\text{BHAR}}$ uncertainties) in the bottom panel. This is because, at $z \lesssim 1$, even for the highest M_{halo} shown, the corresponding $\log M_{\star}$ is below 11.5.

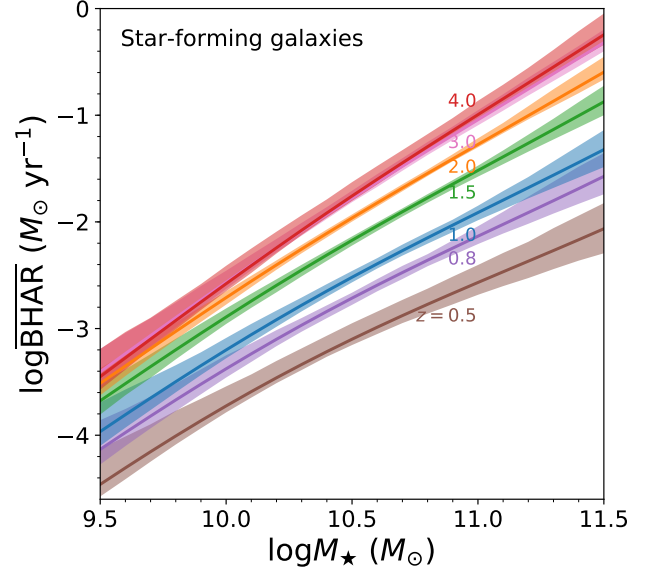


Figure 10. Same format as Fig. 9 (top) but for star-forming galaxies only. We do not show $\log M_{\star} > 11.5$ due to large uncertainties. The BHAR dependence on M_{\star} does not become significantly weaker toward low redshift.

the two scenarios are similar at $\log M_{\star} \lesssim 11.5$ ($\overline{\text{BHAR}}$ differences $\lesssim 0.3$ dex). We thus only discuss the $\overline{\text{BHAR}}(M_{\star}, z)$ for star-forming galaxies at $\log M_{\star} \lesssim 11.5$. The results for the first scenario are displayed in Fig. 10.

The $\overline{\text{BHAR}}$ dependence on M_{\star} does not become significantly weaker toward low redshift. Therefore, it is likely that the shallow slope of the $\overline{\text{BHAR}}\text{--}M_{\star}$ relation for all galaxies in §3.4.1 is due to the increasing fraction of quiescent galaxies toward low redshifts and high M_{\star} . However, one caveat is that our star-forming vs. quiescent classification scheme is largely empirical (§2.1). Previous studies adopt various criteria for identifying star-forming galaxies (e.g., Elbaz et al. 2011; Laigle et al. 2016), while the physical meanings of these bimodal classification schemes are still under debate (e.g., Feldmann 2017). Different classification methods can yield different $\overline{\text{BHAR}}\text{--}M_{\star}$ relations in Fig. 10.

3.4.3 Quiescent Galaxies

We have tested deriving $\overline{\text{BHAR}}$ for quiescent galaxies. However, the uncertainties are generally large, and thus we do not show the results. The large uncertainties are due to the limited sample size of quiescent galaxies, especially in the high- z and low- M_{\star} regime ($z \gtrsim 2$ and $\log M_{\star} \lesssim 10.5$; see §3.4.2). At low redshifts and high M_{\star} , $\overline{\text{BHAR}}$ is also significantly affected by whether to include BL AGNs as quiescent galaxies (see §3.4.2).

3.5 Reliability Checks

3.5.1 Effects of X-ray Obscuration

In §2.1, we derived L_{X} from observed-frame hard-band fluxes. However, even these measurements might suffer from

obscuration, and thus the inferred L_X might be underestimated. Also, we assume a photon index of 1.6 when deriving L_X , and this choice could introduce additional uncertainties.

To evaluate the accuracy of our L_X estimations, we compare them with those derived from XSPEC spectral fitting (e.g., Arnaud 1996). This exercise is performed for GOODS-S sources for which we have L_X from X-ray spectral fitting (see §2.3 in Yang et al. 2017 for details of the spectral fitting). The intrinsic obscuration column density and photon index are free parameters in the fitting. The L_X values derived from fluxes agree well with those derived from spectral fitting: the systematic offset is 0.01 dex, and the typical offset (the median of $|\Delta \log L_X|$) is 0.09 dex. We do not find significant redshift or luminosity dependence of the systematic offset, indicating that our adopted L_X values should also be reliable for COSMOS AGNs which are generally more luminous than GOODS-S AGNs.

At $z > 2$, assuming $\Gamma = 1.8$ instead of $\Gamma = 1.6$ leads to a systematic overestimation (≈ 0.1 dex) of L_X compared to that derived from spectral fitting, likely because Γ appears generally lower at high redshift (e.g., Marchesi et al. 2016b). At low redshift where the k correction is smaller, the flux-based L_X is only weakly dependent on Γ ; for example, at $z = 1$, the difference between L_X produced by $\Gamma = 1.6$ and $\Gamma = 1.8$ is only 0.04 dex. The relatively low apparent value of Γ (1.6) at high redshift might result from Compton reflection. At $z \gtrsim 2$, the X-ray observations can cover energies above 20 keV where the Compton reflection component is strong. The reflection component is hard, and thus may cause the “apparent” Γ value to be lower than the “intrinsic” value. However, due to the limited number of counts, it not feasible to model properly the reflection component and obtain the “intrinsic” Γ . Our adopted $\Gamma = 1.6$ is thus a practical approximation for the total X-ray spectra rather than necessarily the intrinsic photon index for the transmission component.

Most of the distant AGNs detected in X-ray surveys are likely Compton-thin (CTN; $N_{\text{H}} < 10^{24} \text{ cm}^{-2}$; e.g., Liu et al. 2017), and the XLF we adopt does not include Compton-thick (CTK) AGNs. Therefore, our derived $\overline{\text{BHAR}}(M_\star, z)$ does not account for accretion contributed by CTK AGNs. Previous studies indicate that the CTK population is unlikely to be dominant over other AGNs and there is no evidence that the CTK fraction strongly depends on M_\star and/or z . (e.g., Gilli et al. 2007; Treister et al. 2009; Buchner et al. 2015; Ricci et al. 2015; Akylas et al. 2016; Baronchelli et al. 2017). Thus, our $\overline{\text{BHAR}}(M_\star, z)$ should not be significantly affected by CTK AGNs.

3.5.2 Contamination from X-ray Binaries

In the low- L_{SX} regime, the X-ray sources have a significant contribution of X-ray emission from XRBs rather than AGNs. X-ray emission from XRBs can be modeled as $L_{\text{SX,XRB}} = \alpha M_\star + \beta \text{SFR}$, where α and β are functions of redshift. We adopt α and β from model 269 of Fragos et al. (2013) which is preferred by the observations of Lehmer et al.

(2016). Therefore, the L_{SX} for XRBs can be written as

$$\begin{aligned} L_{\text{SX,XRB}} &= \frac{L_{\text{X,XRB}}}{M_\star} \\ &= \frac{\alpha M_\star + \beta \text{SFR}}{M_\star} \\ &= \alpha + \beta \text{sSFR}. \end{aligned} \quad (18)$$

Since most star-forming galaxies have similar sSFR at a given redshift (i.e., the star-forming “main sequence”), the right-hand side of Eq. 18 only depends on redshift for star-forming galaxies. For quiescent galaxies, the $L_{\text{SX,XRB}}$ is even lower than that of star-forming galaxies. We display the $L_{\text{SX,XRB}}$ for the main-sequence galaxies as a function of redshift in Fig. 3 (bottom). The sSFR is from Eq. 13 of Elbaz et al. (2011). The $L_{\text{SX,XRB}}$ increases toward higher redshift. Above our L_{SX} threshold ($\log L_{\text{SX}} = -2$; see §3.2.3), all the sources have L_{SX} larger than $L_{\text{SX,XRB}}$. Even for the GOODS-S data (the deepest), the typical L_{SX} of our X-ray AGNs is higher than $L_{\text{SX,XRB}}$ by an order of magnitude at any redshift. Also, almost all of our X-ray sources above $\log L_{\text{SX}} = -2$ in GOODS-S (98%) and GOODS-N (99%) are classified as “AGN” instead of “galaxy” by Luo et al. (2017) and Xue et al. (2016), respectively. Therefore, our analyses should not be significantly affected by X-ray emission from XRBs.

3.5.3 Sample M_\star Completeness

To evaluate potential issues of M_\star completeness, we derive the galaxy comoving number density as a function of M_\star for each field and compare with the SMF from Behroozi et al. (2013, see §2.2). The number density is calculated as the observed number of galaxies divided by the corresponding comoving volume. Fig. 11 displays the results for $z = 3-4$ (the highest redshift range probed in this work). The number densities for all the three fields agree with the SMF above $\log M_\star = 9.5$ (our M_\star cut; see §3.2.2), indicating our sample is complete for the M_\star regime probed in this work. The number density for COSMOS deviates from the SMF below $\log M_\star \approx 9$. The number densities for GOODS-S and GOODS-N both deviate from the SMF below $\log M_\star \approx 8.5$, as expected from their deeper imaging data than those of COSMOS.

3.5.4 Contribution to $\overline{\text{BHAR}}$ from Low- L_{SX} Accretion

Our derivation of $\overline{\text{BHAR}}$ does not include the contribution from $\log L_{\text{SX}} < -2$ (see §3.2.3 and §3.4.1). Although we have shown that this low- L_{SX} accretion cannot contribute significantly to the overall SMBH growth (see §3.2.3), it can still affect the $\overline{\text{BHAR}}-M_\star$ relation, especially at low redshifts when the $\overline{\text{BHAR}}$ from high- L_{SX} accretion is low.

We here consider one extreme case in which $P(L_{\text{SX}}|M_\star, z)$ is a narrow lognormal distribution centered at $\log L_{\text{SX}} = -2.2$ with a width of ± 0.1 dex; then the $\overline{\text{BHAR}}$ contribution from $\log L_{\text{SX}} < -2$ will be dominant over that from $\log L_{\text{SX}} \geq -2$. This extreme case can be used to estimate the upper limit on $\overline{\text{BHAR}}$ contributed by $\log L_{\text{SX}} < -2$.

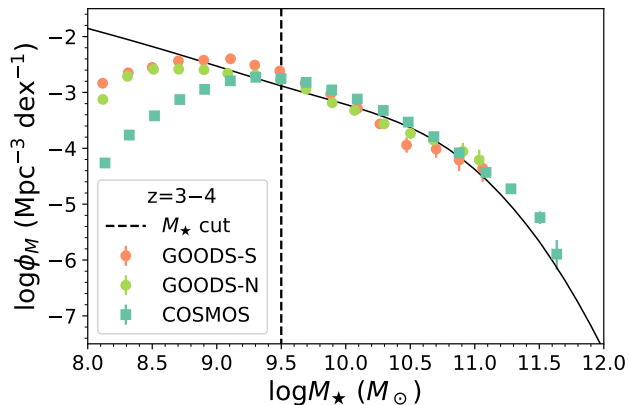


Figure 11. Galaxy comoving number density as a function of M_* at $z = 3.0-4.0$. The data points indicate values derived from our sample of different fields. We do not plot bins where only one source is available due to large uncertainties. The black solid curve represents the SMF from Behroozi et al. (2013). The vertical black dashed line indicates our M_* cut (see 3.2.2). Our sources in all of the three fields are complete above our M_* cut.

Quantitatively, we can estimate this upper limit as

$$\begin{aligned} \overline{\text{BHAR}} &= \frac{L_X k_{\text{bol}} (1 - \epsilon)}{\epsilon c^2} \\ &= \frac{L_{\text{SX}} k_{\text{bol}} (1 - \epsilon)}{\epsilon c^2} M_* \\ &\approx 10^{-3.5} \frac{M_*}{10^{10} M_\odot}, \end{aligned} \quad (19)$$

where we adopt $\epsilon = 0.1$ and $k_{\text{bol}} = 10$ (see §3.2.3). Only at low redshifts ($z \lesssim 0.8$), can our $\overline{\text{BHAR}}$ (see Fig. 9) be below this upper limit. Therefore, low- L_{SX} accretion can only be important at low redshifts.

To examine whether low- L_{SX} accretion is actually dominant over high- L_{SX} accretion at low redshifts, we utilize GOODS-S where the deepest X-ray observations and stacking data are available to probe low- L_{SX} accretion (e.g., Vito et al. 2016; Yang et al. 2017). We study sources in three M_* bins ($\log M_* = 9.5-10$, $10-10.5$, and $10.5-11$) at $z = 0.4-0.7$. We do not probe higher M_* due to the limited number of galaxies (only 14 available). We use total L_X to approximate total BHAR for each M_* bin. For each M_* bin, we obtain the total L_X for all sources in this bin, including both X-ray detected and undetected sources (via stacking); we also derive the contributions to total L_X from $\log L_{\text{SX}} \geq -2$ sources by summing the L_X of detected X-ray sources above $\log L_{\text{SX}} = -2$. We find that, for all of the three M_* bins, the contributions from $\log L_{\text{SX}} \geq -2$ sources account for $\gtrsim 80-90\%$ of the total L_X . If we only consider the L_X from AGNs by subtracting the expected XRB component (see Eq. 1 of Yang et al. 2017), almost all ($\gtrsim 99\%$) of the total L_X from AGNs is from $\log L_{\text{SX}} \geq -2$ sources. The dominance of accretion at $\log L_{\text{SX}} \geq -2$ indicates that the extreme lognormal $P(L_{\text{SX}}|M_*, z)$ distribution above is unlikely to be physical, which is also suggested by some other studies (e.g., Aird et al. 2017a; Georgakakis et al. 2017).

Therefore, we conclude that accretion from sources with $\log L_{\text{SX}} < -2$, which is not included in our $\overline{\text{BHAR}}$ calcula-

tion, should not significantly affect our $\overline{\text{BHAR}}(M_*, z)$ at all redshifts probed (i.e., $z = 0.4-4$).

3.5.5 Bolometric Correction

The analyses in §3.4 assume k_{bol} is a function of L_X . This luminosity-dependent k_{bol} is generally larger for more massive galaxies, as they typically host AGNs with higher L_X (e.g., Aird et al. 2017a; Yang et al. 2017). However, k_{bol} might be related to λ_{Edd} (see §2.3).

If we assume a $k_{\text{bol}}-\lambda_{\text{Edd}}$ relation instead, then the k_{bol} dependence on M_* will be weaker, because, compared to L_X , λ_{Edd} is likely much less dependent on M_* (e.g., Aird et al. 2012; Lusso et al. 2012; Aird et al. 2017a). We test an extreme case such that k_{bol} is a constant value of 22.4 (the median of k_{bol} values in the local AGN sample of Vasudevan & Fabian 2007). The resulting $\overline{\text{BHAR}}(M_*, z)$ is broadly similar to that in Fig. 9. $\overline{\text{BHAR}}$ generally has positive dependence on M_* and redshift, and the redshift dependence is stronger in more massive systems. However, we find that the $\overline{\text{BHAR}}-M_*$ relation becomes flat at $z \lesssim 1.0$ and $\log M_* \gtrsim 11.5$. This redshift and M_* regime is marked in Fig. 9 (see also Appendix B).

4 DISCUSSION

4.1 Physical Causes of the $\overline{\text{BHAR}}-M_*$ Relation and its Cosmic Evolution

At a given M_* , $\overline{\text{BHAR}}$ is positively correlated with redshift out to $z \approx 4$ (see Fig. 9). The physical reason could be that cold gas which fuels SMBH growth becomes more abundant toward high redshift (e.g., Mullaney et al. 2012; Popping et al. 2012; Vito et al. 2014a). At a given redshift, $\overline{\text{BHAR}}$ is generally higher in massive galaxies. As discussed in §4.2 of Yang et al. (2017), this positive dependence of BHAR on M_* might be due to, e.g., deeper potential wells (e.g., Bellovary et al. 2013) and/or higher SMBH occupation fractions at high M_* (e.g., Volonteri 2010).

The positive dependence of $\overline{\text{BHAR}}$ on M_* becomes significantly weaker at low redshift, i.e., the $\overline{\text{BHAR}}-M_*$ slope becomes shallower. One possible cause of the shallower BHAR- M_* slope at low redshifts is that the fraction of star-forming galaxies, which have generally stronger AGN activity than quiescent galaxies, decreases toward low redshift and high- M_* . We show that when only including star-forming galaxies, the $\overline{\text{BHAR}}-M_*$ slope does not become significantly shallower at low redshifts (see §3.4.2).

The low $\overline{\text{BHAR}}$ of massive galaxies at low redshift is understandable considering the cosmic evolution of the SMF and XLF. Luminous quasars ($\log L_X \gtrsim 44$), which are likely responsible for most of the SMBH growth in massive galaxies (e.g., Marconi et al. 2004), become much rarer toward the local universe (e.g., Schmidt 1968; Ueda et al. 2014). The number density of massive galaxies, however, becomes higher toward low redshift (see, e.g., Fig. 15 of Davidzon et al. 2017). Therefore, the average SMBH accretion power for the massive galaxy population decreases sharply toward low redshift. The strong redshift dependence of BHAR for massive galaxies is also evident in our survey data. The detected AGN fraction ($\log L_{\text{SX}} > -2$) is $\approx 9\%$ among massive

galaxies ($\log M_\star > 11$) at $z > 2$, while the fraction is $\approx 5\%$ at $z < 2$. Considering the larger incompleteness at higher redshift, the intrinsic AGN fractions for $z > 2$ and $z < 2$ should have even larger differences.

The physical cause of this strong $\overline{\text{BHAR}}$ redshift evolution might be AGN feedback that could regulate the growth of SMBHs in massive galaxies. At high redshift, effective quasar-mode accretion could launch powerful winds that expel the cold gas in host galaxies (e.g., King & Pounds 2015). Due to the lack of cold gas, SMBH growth drops significantly toward low redshift and hot-gas accretion occurs. The hot accretion flow could produce jets that prevent the gas from cooling and thereby maintain a low accretion rate (e.g., Croton et al. 2006; Yuan & Narayan 2014).

The positive dependence of $\overline{\text{BHAR}}$ on redshift (especially at $z \gtrsim 2$) does not contradict the observational fact that ρ_{BHAR} peaks at $z \approx 2$ (e.g., Brandt & Alexander 2015). We calculate ρ_{BHAR} by convolving BHAR with the SMF, i.e.,

$$\rho_{\text{BHAR}}(z) = \int_{9.5}^{12} \overline{\text{BHAR}}(M_\star, z) \phi_M(M_\star | z) d \log M_\star. \quad (20)$$

Fig. 12 (top) displays the results. The $z \approx 2$ peak is successfully reproduced. $\overline{\text{BHAR}}$ describes the accretion power *per galaxy* while ρ_{BHAR} characterizes the accretion power per comoving volume. Their different redshift evolution indicates that the drop of ρ_{BHAR} toward high redshift is driven by the evolution of the SMF: the number density of galaxies with $\log M_\star \approx 9.5\text{--}12$ decreases toward high redshift (e.g., Davidzon et al. 2017). A similar conclusion is also found by Vito et al. (2017) who studied X-ray AGNs at $z = 3\text{--}6$. Our ρ_{BHAR} curve has a similar shape as that of Ueda et al. (2014, see their Fig. 20), but it is a factor of ≈ 3 lower than theirs. The difference is primarily caused by the different k_{bol} adopted: our k_{bol} (from Lusso et al. 2012; §2.3) is ≈ 3 times lower than their k_{bol} (from Hopkins et al. 2007) at $\log L_X \approx 44$ (the XLF break luminosity). For the reasons explained in §2.3, we believe our adopted k_{bol} is more reliable than that from Hopkins et al. (2007).

Some studies suggest that M_{BH} might be fundamentally related to the mass of the dark matter halo (M_{halo} ; e.g., Ferrarese 2002; but also see Kormendy & Ho 2013). We thus change the variable M_\star to M_{halo} utilizing the typical redshift-dependent $M_{\text{halo}}\text{--}M_\star$ relation from Behroozi et al. (2013, see their Fig. 7), and convert $\overline{\text{BHAR}}(M_\star, z)$ to $\overline{\text{BHAR}}(M_{\text{halo}}, z)$. Fig. 9 (bottom) displays the results.⁶ At $\log M_{\text{halo}} \lesssim 12\text{--}13$, $\overline{\text{BHAR}}$ is positively dependent on M_{halo} and strongly so at high redshifts. At higher M_{halo} , $\overline{\text{BHAR}}$ becomes relatively flat as a function of M_{halo} , indicating M_{halo} is not a good tracer of BHAR in massive systems (e.g., Kormendy & Ho 2013).

To clarify the cause of this flatness, we express the slope of the $\overline{\text{BHAR}}\text{--}M_{\text{halo}}$ relation as

$$\frac{d \log \overline{\text{BHAR}}}{d \log M_{\text{halo}}} = \frac{d \log \overline{\text{BHAR}}}{d \log M_\star} \frac{d \log M_\star}{d \log M_{\text{halo}}}. \quad (21)$$

The slope of the $M_\star\text{--}M_{\text{halo}}$ relation ($d \log M_\star / d \log M_{\text{halo}}$) is small ($\lesssim 0.3$) above $\log M_{\text{halo}} \approx 12\text{--}13$ (see Fig. 7 of Behroozi

⁶ Due to the complicated evolution history of massive systems (e.g., frequent mergers), Behroozi et al. (2013) do not provide relations such as $M_{\text{halo}}\text{--}M_\star$ and $\text{SFR}\text{--}M_\star$ at very high M_\star (P. Behroozi 2017, private communication).

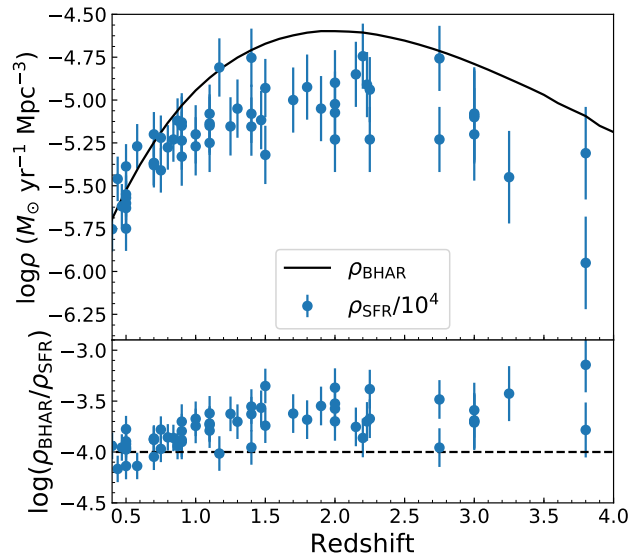


Figure 12. Top panel: ρ_{BHAR} and ρ_{SFR} as a function of redshift. The black solid curve indicates ρ_{BHAR} derived from our best-fit model using Eq. 20; the blue data points indicate ρ_{SFR} scaled by a factor of 10^{-4} (Behroozi et al. 2013). Bottom panel: the $\rho_{\text{BHAR}}/\rho_{\text{SFR}}$ ratio as a function of redshift. The black horizontal dashed line represents a constant ratio of 10^{-4} . $\rho_{\text{BHAR}}/\rho_{\text{SFR}}$ depends on redshift weakly.

et al. 2013), and this results in a small slope of the $\overline{\text{BHAR}}\text{--}M_{\text{halo}}$ relation ($d \log \overline{\text{BHAR}} / d \log M_{\text{halo}}$), even though the $\overline{\text{BHAR}}\text{--}M_\star$ relation can be steep (e.g., $d \log \overline{\text{BHAR}} / d \log M_\star \gtrsim 1$ at $z \gtrsim 1$; see Fig. 9 top). The physical cause of the flat $M_\star\text{--}M_{\text{halo}}$ relation in massive systems is likely that gas cannot efficiently cool and collapse to form stars. This inefficient cooling might be due to AGN feedback and/or deep gravitational potential wells in massive halos (e.g., Rees & Ostriker 1977; §8.4 of Kormendy & Ho 2013).

4.2 BHAR vs. SFR

The redshift-evolution curves of ρ_{BHAR} and ρ_{SFR} are similar at least up to $z \approx 2$ (e.g., Kormendy & Ho 2013; Aird et al. 2015; Fig. 12, which we will discuss in detail below). This similarity is considered a supporting point of the straightforward scenario that the long-term growth of SMBHs and their host galaxies are in lockstep. However, ρ_{BHAR} and ρ_{SFR} are quantities averaged over the whole galaxy population from low M_\star to high M_\star , and their evolutionary similarity might not hold for galaxies with different M_\star .

To investigate this possibility, we compare the $\overline{\text{BHAR}}\text{--}M_\star$ relation with the $\text{SFR}\text{--}M_\star$ relation from Behroozi et al. (2013) in Fig. 13 (top). The $\text{SFR}\text{--}M_\star$ relation is truncated at high M_\star due to the reason in Footnote 6. We note that the $\overline{\text{SFR}}\text{--}M_\star$ relation represents an ensemble-averaged property (the same as for the $\overline{\text{BHAR}}\text{--}M_\star$ relation), and thus it is not affected by the SFR variability of individual galaxies. We normalize the SFR values by a factor of 10^{-4} so that they become comparable with $\overline{\text{BHAR}}$. Fig. 13 (bottom) presents the $\overline{\text{BHAR}}/\overline{\text{SFR}}$ ratio as a function of M_\star .

At a given M_\star , both $\overline{\text{BHAR}}$ and $\overline{\text{SFR}}$ rise toward high

redshifts in general. However, $\overline{\text{BHAR}}/\overline{\text{SFR}}$ has relatively weak redshift evolution, especially at $z \gtrsim 0.8$. At a given redshift, $\overline{\text{BHAR}}$ rises more strongly as a function of M_\star than $\overline{\text{SFR}}$. As a result, the $\overline{\text{BHAR}}/\overline{\text{SFR}}$ ratio is positively correlated with M_\star at a given redshift, broadly consistent with the findings of Yang et al. (2017, the data points in Fig. 13 bottom). This positive dependence disfavors the straightforward coevolution model where SMBH and galaxy growth are in lockstep and $\overline{\text{BHAR}}/\overline{\text{SFR}}$ is a universal constant (e.g., Hickox et al. 2014). As explained in §4.2 of Yang et al. (2017), the larger $\overline{\text{BHAR}}/\overline{\text{SFR}}$ toward high M_\star may indicate that massive systems are more effective in feeding cold gas to their central SMBHs due to, e.g., their deep potential wells. Another possibility is that the SMBH occupation fraction increases toward high M_\star . Our $\overline{\text{BHAR}}/\overline{\text{SFR}}$ agrees with the sample of Yang et al. (2017) at $0.5 \leq z < 1.3$ (the red points in Fig. 13). We do not compare with their high-redshift ($1.3 \leq z < 2.0$) sample, because luminous AGNs ($\log L_X \gtrsim 44$) are dominant at high redshift but almost absent in their sample. This rarity of luminous AGNs is due to the small area of GOODS-S used in Yang et al. (2017) and the removal of BL AGNs from their sample.

Fig. 12 compares our ρ_{BHAR} (§4.1) with ρ_{SFR} from the observational data compiled by Behroozi et al. (2013). The ρ_{BHAR} and ρ_{SFR} curves have similar shapes consistent with previous work (e.g., Kormendy & Ho 2013; Aird et al. 2015). The $\rho_{\text{BHAR}}/\rho_{\text{SFR}}$ ratio only rises slightly (≈ 0.3 dex) from $z = 0$ to $z \gtrsim 3$. We note that this weak redshift dependence does not contradict our conclusion that $\overline{\text{BHAR}}/\overline{\text{SFR}}$ for massive galaxies ($\log M_\star \gtrsim 11$) rises strongly toward high redshift (see Fig. 13). This is because massive galaxies are relatively rare and their weight in $\rho_{\text{BHAR}}/\rho_{\text{SFR}}$ is not dominant over that of less-massive galaxies.

Fig. 14 compares the $\overline{\text{BHAR}}-M_\star$ and $\overline{\text{SFR}}-M_\star$ relations for star-forming galaxies. The $\overline{\text{SFR}}$ vs. M_\star are from the star-forming main-sequence relations (Eq. 6 of Aird et al. 2017b). We do not compare these relations above $z = 3$, as the uncertainties of the main-sequence relations are large at $z \gtrsim 3$. At a given redshift, the $\overline{\text{SFR}}-M_\star$ relation generally has a slope shallower than the $\overline{\text{BHAR}}-M_\star$ relation. This leads to $\overline{\text{BHAR}}/\overline{\text{SFR}}$ rising toward high M_\star (Fig. 14 bottom), similarly to the trend in Fig. 13 (bottom). Also similarly to Fig. 13 (bottom), the $\overline{\text{BHAR}}/\overline{\text{SFR}}$ has weak redshift evolution at a given M_\star above $z \gtrsim 0.8$. The $\overline{\text{BHAR}}/\overline{\text{SFR}}$ curve in Fig. 14 is concave down while that in Fig. 13 is concave up.

Fig. 14 also shows the $\overline{\text{BHAR}}/\overline{\text{SFR}}$ measurements from the literature. The $\overline{\text{BHAR}}/\overline{\text{SFR}}$ values from Mullaney et al. (2012) are higher than ours, possibly due to their large uncertainties. However, the observations of Rodighiero et al. (2015) at $z \sim 2$ have much smaller uncertainties and agree with our $\overline{\text{BHAR}}/\overline{\text{SFR}}$. Since these measurements are for star-forming galaxies, they are not displayed in Fig. 13, which is for all galaxies.

4.3 Evolution of The $M_{\text{BH}}-M_\star$ Relation

Our $\overline{\text{BHAR}}(M_\star, z)$ describes the long-term average BHAR for a galaxy at given M_\star and z . Based on $\overline{\text{BHAR}}(M_\star, z)$, we can calculate the cumulative accreted SMBH mass for galaxies

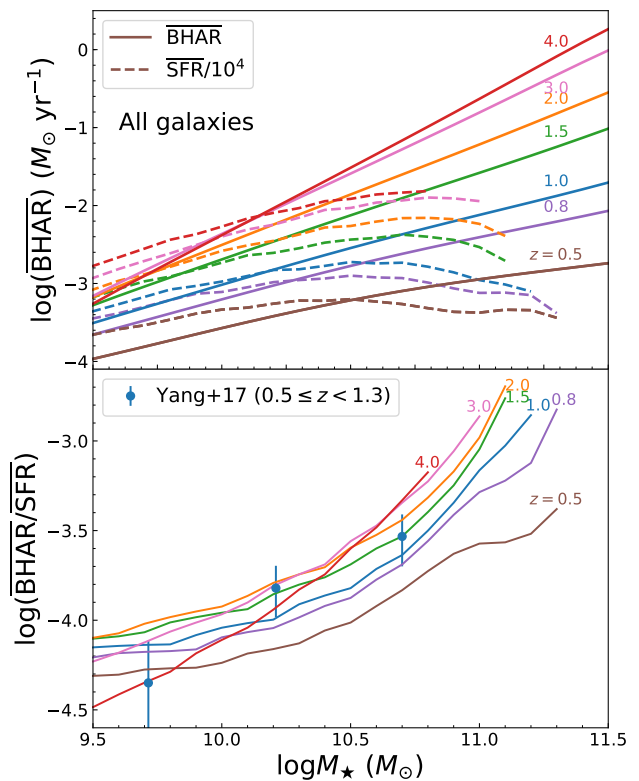


Figure 13. Top panel: Comparison between $\overline{\text{BHAR}}$ and $\overline{\text{SFR}}$ as functions of M_\star . The solid lines indicate BHAR; the dashed lines indicate $\overline{\text{SFR}}$ scaled by a factor of 10^{-4} . Different colors indicate different redshifts as labeled. Bottom panel: The ratio between $\overline{\text{BHAR}}$ and $\overline{\text{SFR}}$ as functions of M_\star at different redshifts. The purple data points indicate the measured $\overline{\text{BHAR}}/\overline{\text{SFR}}$ values from Yang et al. (2017). At $z \gtrsim 0.5$, $\overline{\text{BHAR}}/\overline{\text{SFR}}$ rises toward high M_\star ; it is flat as a function of M_\star at lower redshift.

with given stellar mass history $[M_\star(z)]$, i.e.,

$$M_{\text{BH}}(z) = \int_4^z \overline{\text{BHAR}}(M_\star(z'), z') \frac{dt}{dz'} dz' + M_{\text{BH}}|_{z=4}, \quad (22)$$

where t is the cosmic time; the prime superscript in z' is to differentiate the redshift z as the integral upper boundary. We adopt the stellar mass history of Behroozi et al. (2013) who derived the average $M_\star(z)$ for galaxies as a function of $M_\star(z=0)$ up to $\log M_\star(z=0) \approx 11.4$ (see their Fig. 9). To obtain the initial condition $M_{\text{BH}}|_{z=4}$, we test different $M_{\text{BH}}/M_\star|_{z=4}$ values and multiply them with $M_\star(z=4)$ from Behroozi et al. (2013).

When $M_\star(z)$ lies below our limit of $\log M_\star = 9.5$ in Eq. 22 (i.e., our M_\star cut; see §3.2.2), we assume their $\overline{\text{BHAR}}$ as $\overline{\text{BHAR}}(\log M_\star = 9.5, z) \times (M_\star/10^{9.5})^\zeta$. We set the power-law index $\zeta = 1$, i.e., assuming $\overline{\text{BHAR}}$ at $\log M_\star \leq 9.5$ is proportional to $\overline{\text{BHAR}}$ at $\log M_\star = 9.5$ (e.g., §3.2 of Yang et al. 2017). To reduce the uncertainties of this approximation, we do not discuss the $M_{\text{BH}}-M_\star$ relation for $\log M_\star < 10$ at all redshifts.⁷ In fact, we find that setting ζ to 0.5 or

⁷ We still need to assume $\overline{\text{BHAR}}$ for $\log M_\star \leq 9.5$, even though we do not probe $\log M_\star < 10$. For example, a galaxy with $\log M_\star(z =$

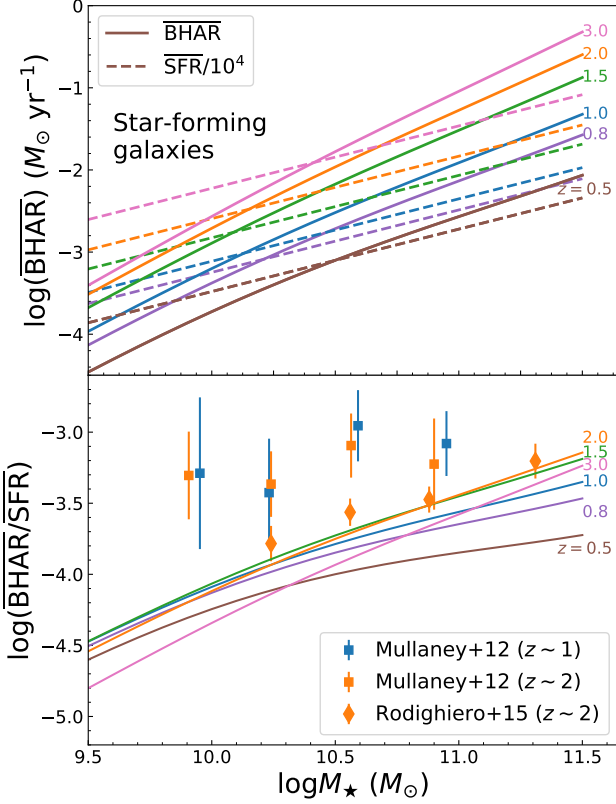


Figure 14. Same format as Fig. 13 but for star-forming galaxies only. The data points in the bottom panel indicate measurements from Mullaney et al. (2012); Rodighiero et al. (2015).

2 does not affect our conclusions. For redshifts below our cut ($z = 0.4$; §3.2.1), we use $\overline{\text{BHAR}}$ from model extrapolation. This should not bring noticeable uncertainties given that $\overline{\text{BHAR}}$ is low at $z < 0.4$. In fact, we have tested two extreme scenarios: $\overline{\text{BHAR}}(M_\star, z < 0.4) = \overline{\text{BHAR}}(M_\star, z = 0.4)$ (no redshift evolution at $z < 0.4$) and $\overline{\text{BHAR}} = 0$ (no SMBH growth at $z < 0.4$), respectively. Both of these cases produce almost the same $M_{\text{BH}}-M_\star$ relation as that from model extrapolation.

In Eq. 22, we assume long-term BHAR can be inferred from M_\star and redshift. This assumption will not be strictly correct, if, for example, $\overline{\text{BHAR}}$ also depends on SFR at given M_\star and redshift. However, this SFR dependence is likely weak based on previous work (e.g., Stanley et al. 2017; Yang et al. 2017), and significantly different $\overline{\text{BHAR}}$ might only be found between galaxies with extremely different SFRs, e.g., star-forming vs. quiescent galaxies (e.g., Aird et al. 2017a; Wang et al. 2017). In the case of weak SFR dependence, our ensemble analyses are still valid in characterizing the typical $M_{\text{BH}}-M_\star$ relation for the entire galaxy population.

We show the resulting M_{BH} as a function of M_\star at different redshifts in Fig. 15. The $M_{\text{BH}}-M_\star$ curves are truncated at the highest $M_\star(z)$ values in Behroozi et al. (2013, see Footnote 6). As expected, the effects of the $M_{\text{BH}}/M_\star|_{z=4}$

$0) = 10.5$ has $\log M_\star < 9.5$ in the early universe ($z > 2$), and we need to account for its SMBH accretion at $z = 2-4$.

assumption generally become weaker toward low redshift. At $z \lesssim 2$, the $M_{\text{BH}}/M_\star|_{z=4} = 1/100$ (black dashed) and $M_{\text{BH}}/M_\star|_{z=4} = 1/10^4$ (black dash-dotted) curves only differ from the $M_{\text{BH}}/M_\star|_{z=4} = 1/500$ (black solid) curve by $\lesssim 0.3$ dex in vertical direction. Thus, below we only discuss the $M_{\text{BH}}-M_\star$ relations at $z \lesssim 2$.

From Fig. 15, the $M_{\text{BH}}-M_\star$ relation only has weak redshift evolution since $z \approx 2$ (solid black vs. red curves). This result does not contradict Fig. 13 which shows that $\overline{\text{BHAR}}$ and $\overline{\text{SFR}}$ have strong redshift dependence. This is because $\overline{\text{BHAR}}$ and $\overline{\text{SFR}}$ are both low at $z \lesssim 0.8$ compared to at higher redshift. For example, at a given M_\star , the $\overline{\text{BHAR}}$ ($\overline{\text{SFR}}$) at $z = 0.5$ is lower than $\overline{\text{BHAR}}$ ($\overline{\text{SFR}}$) at $z = 3$ by a factor of ≈ 10 . Therefore, the SMBH and galaxy growth at $z \lesssim 0.8$ are not important, and the $M_{\text{BH}}-M_\star$ relation is thus primarily determined by $\overline{\text{BHAR}}/\overline{\text{SFR}}$ at higher redshift. At $z \gtrsim 0.8$, the $\overline{\text{BHAR}}/\overline{\text{SFR}}$ does not have strong redshift dependence at a given M_\star . The weak redshift dependence of the $M_{\text{BH}}-M_\star$ relation is consistent with the observations of Schindler et al. (2016) which show that the ratio between SMBH and stellar mass densities is flat as a function of redshift since $z \approx 5$. Based on observations of BL AGNs, Sun et al. (2015) also found a redshift-independent $M_{\text{BH}}-M_\star$ relation (but also see Merloni et al. 2010).

Since massive galaxies tend to form at high redshifts (§3.4), our result suggests that their SMBHs should follow a similar trend. The massive galaxies ($\log M_\star \gtrsim 11$) at $z \approx 2$ are likely the progenitors of local giant ellipticals for which $M_\star = M_{\text{bulge}}$. Their M_{BH} values are already at the level expected from the local $M_{\text{BH}}-M_{\text{bulge}}$ relation (e.g., Häring & Rix 2004; Kormendy & Ho 2013). This conclusion disfavors the scenario that the local $M_{\text{BH}}-M_{\text{bulge}}$ relation for giant ellipticals mostly formed at low redshift, as proposed in §4.3 of Yang et al. (2017). Their scenario assumes their $\overline{\text{BHAR}}-M_\star$ relation (see Fig. 9) extends to $\log M_\star \gtrsim 11$ and has weak redshift evolution at $z \lesssim 2$, which is inconsistent with our results.

The $M_{\text{BH}}-M_\star$ relations at $z \lesssim 2$ differ significantly from those expected from a constant M_{BH}/M_\star ratio (the brown lines in Fig. 15). The M_{BH}/M_\star ratio is positively related to M_\star : it is $\sim 1/5000$ at $\log M_\star \lesssim 10.5$ and rises to $\sim 1/500$ at $\log M_\star \gtrsim 11.2$. This positive dependence is predicted by Yang et al. (2017, see their §4.3) based on the fact that $\overline{\text{BHAR}}/\overline{\text{SFR}}$ is generally higher toward high M_\star (see Fig. 13).

Fig. 15 also compares our $M_{\text{BH}}-M_\star$ relation with the observations of BL AGNs at $z \gtrsim 0.5$ (Jahnke et al. 2009; Merloni et al. 2010; Bennert et al. 2011; Cisternas et al. 2011; Schramm & Silverman 2013; Sun et al. 2015). At $\log M_\star \gtrsim 11$, these observations agree well with our $M_{\text{BH}}-M_\star$ relation. However, at lower M_\star , the M_{BH} values for BL AGNs are significantly higher than those predicted by our $M_{\text{BH}}-M_\star$ relation. The discrepancies might be caused by selection biases and/or M_{BH} measurement uncertainties. Due to observational sensitivity, the BL AGNs with M_{BH} measured tend to have massive SMBHs, and thus do not well represent the whole galaxy population at given M_\star (e.g., Lauer et al. 2007). The measurements of M_{BH} are based on single-epoch spectra, and large uncertainties (both scatter and biases) exist in these measurements (e.g., Shen 2013). In fact, in the local universe where M_{BH} can be measured for BL AGNs with lower luminosities and normal galaxies,

the observations agree better with our $M_{\text{BH}}-M_{\star}$ relation (see §4.4).

We do not calculate M_{BH} vs. M_{\star} for star-forming galaxies due to the lack of their average stellar mass history (i.e., the needed $M_{\star}(z)$ is not provided by Behroozi et al. 2013 or other works to our knowledge), and we only make qualitative arguments below. Since the cosmic evolution of BHAR/SFR for star-forming galaxies is weak at $z \gtrsim 0.8$ (see §4.2), their $M_{\text{BH}}-M_{\star}$ relation should also have weak dependence on redshift (as explained above for all galaxies). The M_{BH}/M_{\star} likely rises in more massive galaxies where BHAR/SFR is higher. These qualitative conclusions for star-forming galaxies are similar to those for all galaxies (Fig. 15).

4.4 The $M_{\text{BH}}-M_{\star}$ Relation at $z = 0$

Fig. 16 compares our $M_{\text{BH}}-M_{\star}$ relation at $z = 0$ with observations. At $\log M_{\star} \gtrsim 11$ where $M_{\star} \approx M_{\text{bulge}}$, our derived M_{BH} is similar to that expected from the $M_{\text{BH}}-M_{\text{bulge}}$ relations in Häring & Rix (2004) and Kormendy & Ho (2013). However, at lower M_{\star} , our M_{BH} is significantly lower compared to that expected from the $M_{\text{BH}}-M_{\text{bulge}}$ relations. This result is expected, because the bulge components become less dominant and $M_{\text{bulge}}/M_{\star}$ drops toward low M_{\star} (e.g., Kelvin et al. 2014).

SMBH growth can occur via both accretion and mergers. Some studies propose that mergers could be the main channel of SMBH growth for local giant ellipticals, and their $M_{\text{BH}}-M_{\star}$ relation might be a natural result of merger averaging (e.g., Peng 2007; Jahnke & Macciò 2011; §8.5 of Kormendy & Ho 2013). However, the similarity between our $M_{\text{BH}}-M_{\star}$ relation and the $M_{\text{BH}}-M_{\text{bulge}}$ relations at high M_{\star} suggests that accretion is sufficient to produce the observed $M_{\text{BH}}-M_{\star}$ relation in local giant ellipticals, since merger growth is not included in our M_{BH} calculation (Eq. 22).⁸ Also, merger averaging of low- M_{\star} galaxies can only lead to the final M_{BH}/M_{\star} ratio being farther from that observed in giant ellipticals, because M_{BH}/M_{\star} is lower toward low M_{\star} . This argument can also apply to the giant ellipticals beyond our probed M_{\star} limit ($\log M_{\star} \approx 11.4$). Therefore, merger growth might not dominate over accretion growth for giant ellipticals in general. We caution that our scheme describes the ensemble-averaged growth history for SMBHs and galaxies, and it is possible that mergers are dominant in some individual systems.

Fig. 16 displays M_{BH} and M_{\star} values for individual normal galaxies (cyan and red data points). The M_{BH} values are measured via reliable stellar dynamics or megamasers. These data points are mainly based on Tabs. 2 (elliptical galaxies) and 3 (disk galaxies) of Kormendy & Ho (2013) where M_{bulge} values are provided, and the unreliable M_{BH} measurements (the purple rows in these two tables) are discarded. For elliptical galaxies, M_{bulge} equals M_{\star} ; for disk galaxies, we divide

M_{bulge} by the K_s -band bulge-to-total luminosity ratio (B/T ; also provided in Kormendy & Ho 2013) to approximate M_{\star} . The data points also include the recent M_{BH} measurements based on megamasers for three galaxies (Mrk 1029, J0437+2456, and UGC 6093; Greene et al. 2016). These data broadly agree with our $M_{\text{BH}}-M_{\star}$ relation: the typical M_{BH}/M_{\star} is low (one over several thousand) at $\log M_{\star} \lesssim 10.5$ and becomes high (one over several hundred) at $\log M_{\star} \gtrsim 11$. At $10.5 \lesssim \log M_{\star} \lesssim 11$, the observed M_{BH} scatters around that expected from our $M_{\text{BH}}-M_{\star}$ relation, although the scatter of M_{BH} is large at a given M_{\star} .

Fig. 16 also compares our $M_{\text{BH}}-M_{\star}$ relation with measurements for local BL AGNs based on single-epoch spectra or reverberation mapping (Reines & Volonteri 2015). At $\log M_{\star} \lesssim 10.5$, these measurements broadly agree with our $M_{\text{BH}}-M_{\star}$ relation and the measurements for normal galaxies. However, at higher M_{\star} , the M_{BH} for BL AGNs is systematically lower than the M_{BH} for normal galaxies at given M_{\star} . This discrepancy could result from large uncertainties in the M_{BH} measurements for BL AGNs (§4.3). For example, these M_{BH} measurements assume a single virial coefficient “ f ” for all sources, which might have systematic errors up to a factor of a few (e.g., Shen 2013). Another possibility is that the normal galaxies with M_{BH} measurements may not be representative of the entire galaxy population due to selection bias. Shankar et al. (2016) proposed that observations tend to select massive SMBHs for which M_{BH} measurements are achievable. They argued that this selection effect might strongly bias the observed $M_{\text{BH}}-M_{\star}$ relation in the local universe, and they presented an intrinsic $M_{\text{BH}}-M_{\star}$ relation (the green curve in Fig. 16). However, our model M_{BH} does not suffer from this selection bias but is generally higher than that of Shankar et al. (2016) at any given M_{\star} . This discrepancy suggests that the selection bias might not be as strong as they proposed.

Fig. 17 shows the $M_{\text{BH}}-M_{\text{halo}}$ relation converted from our $M_{\text{BH}}-M_{\star}$ relation (see §4.1 for the method). The relation is steep ($M_{\text{BH}} \propto M_{\text{halo}}$; the green dashed line) at $\log M_{\text{halo}} \lesssim 13$, but flattens at higher M_{halo} ($M_{\text{BH}} \propto M_{\text{halo}}^{0.4}$; the red dash-dotted line). This behavior qualitatively agrees with Kormendy & Ho (2013, see their §6.10.2) who assumed $M_{\text{bulge}} \approx M_{\star}$. The flattening is expected from the weak BHAR dependence on M_{halo} in massive systems (see Fig. 9).

5 SUMMARY AND FUTURE PROSPECTS

We have derived $\overline{\text{BHAR}}$ as a function of M_{\star} and redshift for galaxies with $\log M_{\star} = 9.5-12$ and $z = 0.4-4$. Our method is based on survey data from GOODS-S, GOODS-N, and COSMOS, as well as the SMF and XLF from the literature. Our main results are summarized below:

(i) $\overline{\text{BHAR}}$ generally increases toward high M_{\star} at a given redshift (see §3.4.1 and 4.1). This M_{\star} dependence becomes weaker toward the local universe. For example, from $\log M_{\star} = 9.5$ to $\log M_{\star} = 11.5$, $\overline{\text{BHAR}}$ increases by a factor of $\sim 10^3$ at $z \approx 4$ while the factor is only ~ 10 at $z \approx 0.5$. This is probably due to the increasing fraction of quiescent galaxies at low redshift and high M_{\star} , as the BHAR- M_{\star} slope does not become much shallower toward low redshift for star-forming galaxies (see §3.4.2). At a given M_{\star} , $\overline{\text{BHAR}}$ is higher toward high redshift, and this redshift dependence is stronger for

⁸ Our scheme of M_{BH} calculation in Eq. 22 is different from the Sołtan argument (Sołtan 1982). The Sołtan argument considers M_{BH} density which is not affected by mergers. However, our M_{BH} calculation aims to characterize the average behavior for individual galaxies. Both accretion and mergers can contribute to the M_{BH} for individual galaxies, although we only consider the accretion component in Eq. 22.

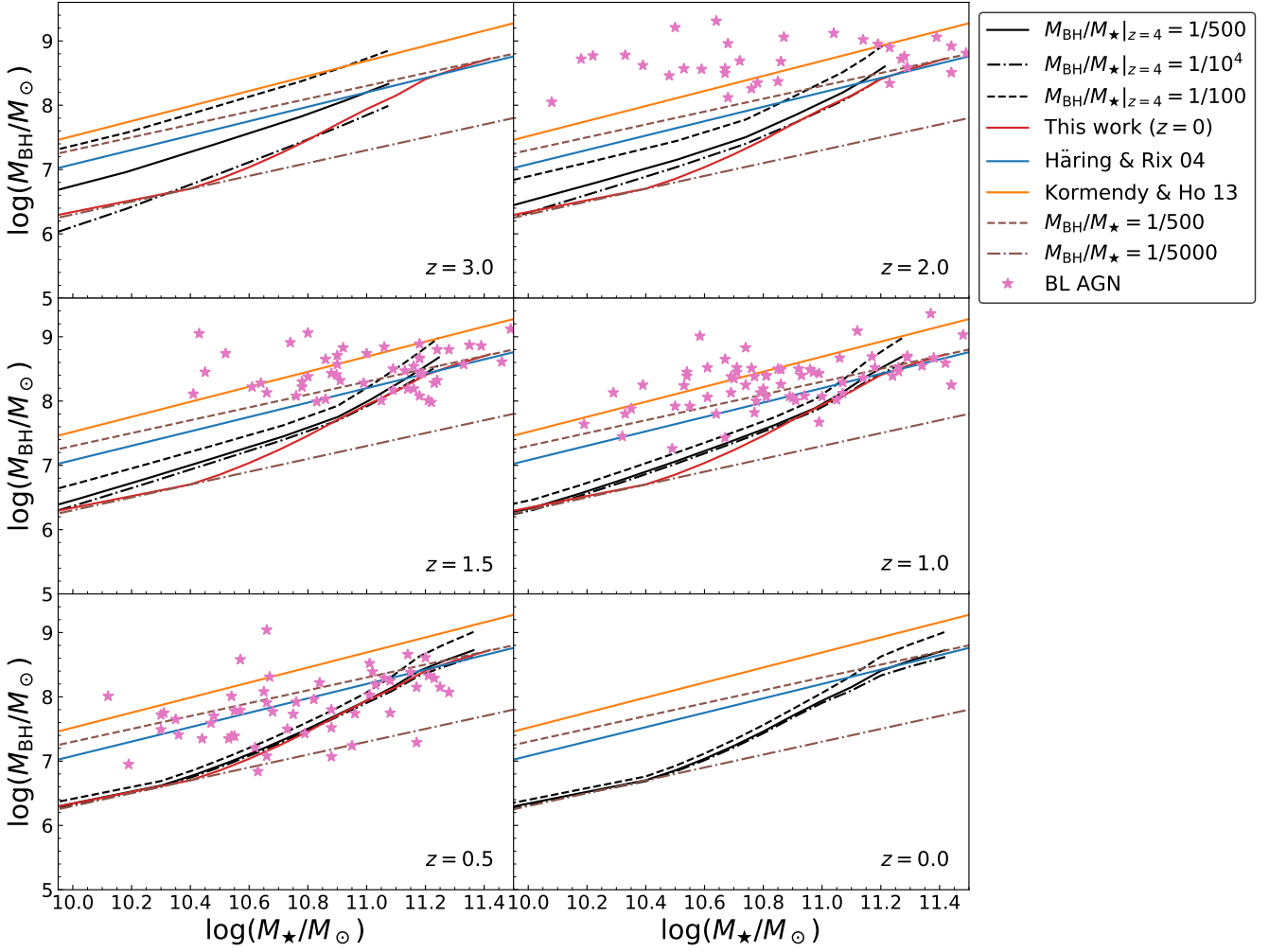


Figure 15. SMBH mass vs. stellar mass at different redshifts. The black solid, dot-dashed, and dashed lines indicate our best-fit model assuming $M_{\text{BH}}/M_\star|_{z=4} = 1/500$, $1/10^4$, and $1/100$, respectively. The MCMC 1σ uncertainties are small ($\lesssim 0.1$ dex) and thus are not shown. The red solid line represents our $M_{\text{BH}}-M_\star$ relation at $z = 0$ assuming $M_{\text{BH}}/M_\star|_{z=4} = 1/500$. The brown dashed and dot-dashed lines are $M_{\text{BH}}/M_\star = 1/500$ and $M_{\text{BH}}/M_\star = 1/5000$, respectively; the blue and orange lines indicate the $M_{\text{BH}}-M_{\text{bulge}}$ relations in the local universe from Häring & Rix (2004) and Kormendy & Ho (2013), respectively. The pink stars identify BL AGNs from the literature (see §4.3). Our $M_{\text{BH}}-M_\star$ relation is not strongly affected by the assumptions about $M_{\text{BH}}/M_\star|_{z=4}$ at $z \lesssim 2$. The $M_{\text{BH}}-M_\star$ relation has weak redshift evolution since $z \approx 2$, and it is similar to the local $M_{\text{BH}}-M_{\text{bulge}}$ relations at high M_\star where $M_\star \approx M_{\text{bulge}}$. At low M_\star , our $M_{\text{BH}}-M_\star$ relation deviates from the $M_{\text{BH}}-M_{\text{bulge}}$ relations likely because the bulge is less dominant toward low M_\star .

more massive systems, e.g., for $\log M_\star \approx 11.5$, $\overline{\text{BHAR}}$ is \approx three decades higher at $z = 4$ than at $z = 0.5$. This strong redshift evolution for massive galaxies is plausibly explained by AGN feedback.

(ii) At a given M_\star , $\overline{\text{BHAR}}/\text{SFR}$ has weak redshift evolution at $z \gtrsim 0.8$. At a given redshift, $\overline{\text{BHAR}}/\text{SFR}$ depends positively on M_\star . These features also exist when limiting the sample to star-forming galaxies. This positive dependence is inconsistent with the scenario that SMBH and galaxy growth are in lockstep. We have converted the $\overline{\text{BHAR}}-M_\star$ relation to the $\overline{\text{BHAR}}-M_{\text{halo}}$ relation based on the recipe of Behroozi et al. (2013). $\overline{\text{BHAR}}$ positively depends on M_{halo} at $\log M_{\text{halo}} \lesssim 12-13$ but becomes flat at higher M_{halo} , indicating SMBH growth is not well traced by M_{halo} in massive systems.

(iii) Based on our $\overline{\text{BHAR}}(M_\star, z)$, $M_\star(z)$ from Behroozi et al. (2013), and the assumption of $M_{\text{BH}}/M_\star|_{z=4}$, we have derived the $M_{\text{BH}}-M_\star$ relation at different redshifts (see §4.3). At $z \lesssim 2$, our $M_{\text{BH}}-M_\star$ relation does not strongly depend on the $M_{\text{BH}}/M_\star|_{z=4}$ assumption. The M_{BH}/M_\star ratio is higher toward massive galaxies: it rises from $\approx 1/5000$ at $\log M_\star \lesssim 10.5$ to $\approx 1/500$ at $\log M_\star \gtrsim 11.2$. Our results suggest the $M_{\text{BH}}-M_\star$ relation is already largely in place at $z \approx 2$. However, the M_{BH} expected from our $M_{\text{BH}}-M_\star$ relation at $\log M_\star \lesssim 11$ is significantly lower than that from the observations of BL AGNs at $z \gtrsim 0.5$. This discrepancy might be due to selection biases and/or inaccuracy of direct M_{BH} measurements of distant BL AGNs.

(iv) Our predicted $M_{\text{BH}}-M_\star$ relation (at $z = 0$) is similar to the local $M_{\text{BH}}-M_{\text{bulge}}$ relation at $\log M_\star \gtrsim 11$, suggesting

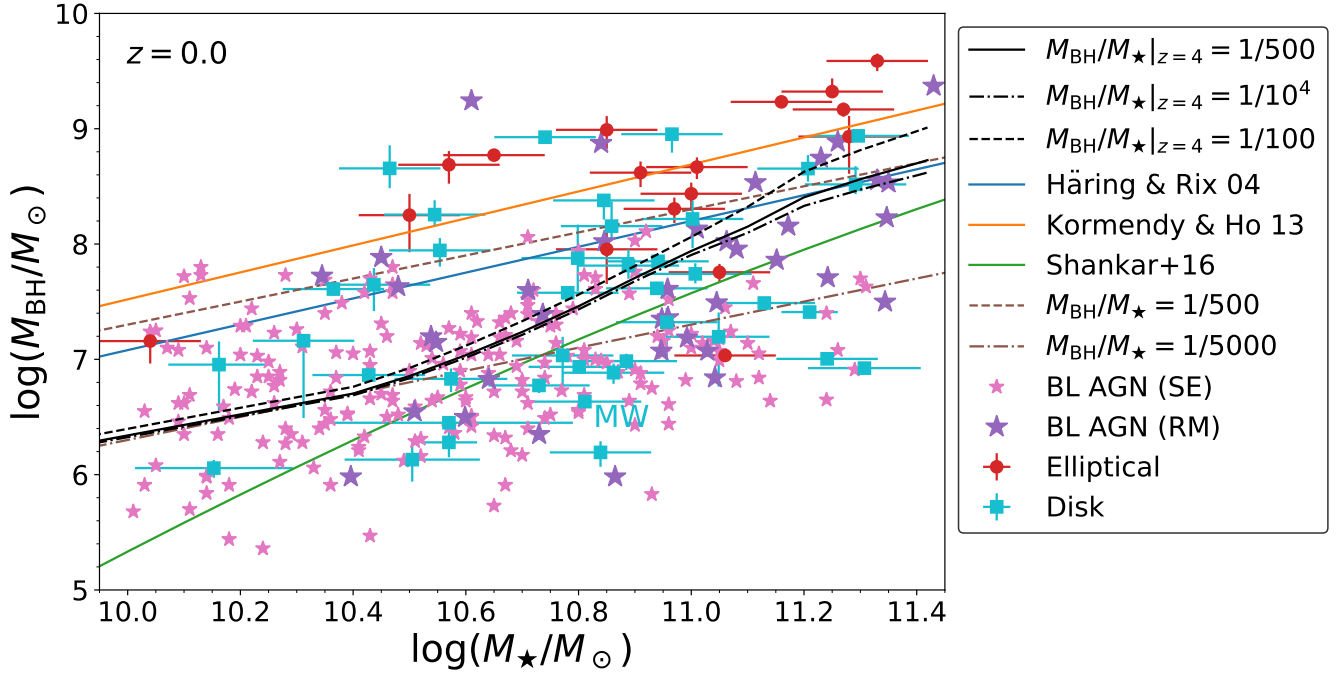


Figure 16. Same format as the bottom-right panel in Fig. 15, but plotted against data points of local systems. The red points and blue squares indicate elliptical and disk galaxies, respectively, with M_{BH} measurements from stellar dynamics or megamasers. The disk galaxies include S0 and spiral galaxies. The data point representing the Milky Way is labeled as “MW” at its lower right. The pink and purple stars represent local BL AGNs based on M_{BH} measurements of single-epoch spectra and reverberation mapping, respectively. The blue and orange lines indicate the $M_{\text{BH}}-M_{\text{bulge}}$ relations from Häring & Rix (2004) and Kormendy & Ho (2013), respectively; the green solid line represents the local “unbiased” $M_{\text{BH}}-M_{\star}$ relation from Shankar et al. (2016).

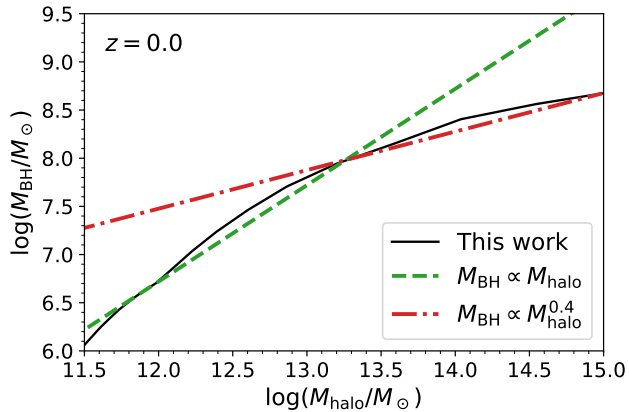


Figure 17. The local $M_{\text{BH}}-M_{\text{halo}}$ relation. The black solid curve indicates our best-fit model assuming $M_{\text{BH}}/M_{\star}|_{z=4} = 1/500$. The curve flattens toward high M_{halo} . The green dashed and red dash-dotted lines indicate $M_{\text{BH}} \propto M_{\text{halo}}$ and $M_{\text{BH}} \propto M_{\text{halo}}^{0.4}$, respectively; they are normalized at $\log M_{\text{halo}} = 12$ and 15, respectively. These two lines are not from fitting but are just to guide the eye.

that mergers do not dominate over accretion in the SMBH growth of giant ellipticals. At $\log M_{\star} \lesssim 10.5$, our $M_{\text{BH}}-M_{\star}$ relation broadly agrees with the observations of local normal galaxies and BL AGNs. At higher M_{\star} , our predicted M_{BH} are broadly consistent with those of normal galaxies but are

systematically higher than those of BL AGNs. We have also derived the $M_{\text{BH}}-M_{\text{halo}}$ relation at $z = 0$ using the $M_{\star}-M_{\text{halo}}$ relation from Behroozi et al. (2013). Similar to the BHAR- M_{halo} relation, $M_{\text{BH}}-M_{\text{halo}}$ relation is steep ($M_{\text{BH}} \propto M_{\text{halo}}$) at $\log M_{\text{halo}} \lesssim 13$ but becomes relatively flat ($M_{\text{BH}} \propto M_{\text{halo}}^{0.4}$) at higher M_{halo} .

In this work, we do not study SMBH growth at $z < 0.4$ due to the limited sample size at low redshifts. Although SMBH accretion in the low- z epoch should not affect the $M_{\text{BH}}-M_{\star}$ relation significantly (see §4.3), it is critical for understanding how SMBH-galaxy coevolution develops from high redshifts to the local universe. Future work could combine wide-field optical/NIR (e.g., SDSS, UKIDSS, and 2MASS) and X-ray (e.g., *Swift*/BAT, *Chandra* Source Catalog, and 3XMM) surveys to investigate the BHAR- M_{\star} relation at low redshift (e.g., Salim et al. 2007; Haggard et al. 2010; Shimizu et al. 2015). We also do not investigate SMBH growth for quiescent galaxies (see §3.4.3); future studies could derive their BHAR- M_{\star} relation.

The scatter of the observed local $M_{\text{BH}}-M_{\star}$ relation is large (Fig. 16). At least one origin of this scatter is related to $M_{\star}(z)$ (see Footnote 5 and Eq. 22). We use average $M_{\star}(z)$ in this work while individual galaxies have different stellar mass histories. This aspect can be investigated based on the $M_{\star}(z)$ for individual systems from numerical simulations such as Illustris (Genel et al. 2014). Another origin of the large scatter may be that BHAR is dependent on other galaxy properties such as SFR, morphology, and cosmic en-

vironment in addition to M_\star (see, e.g., §3.4.2 and [Martini et al. 2009](#); [Kocevski et al. 2012](#); [Aird et al. 2017a](#)). The detailed $\overline{\text{BHAR}}$ dependence on SFR and morphology can be investigated using the CANDELS survey fields where deep *Chandra*, *Herschel*, and *HST* observations are available. The $\overline{\text{BHAR}}$ dependence on environment can be studied using surveys of several deg^2 such as COSMOS and X-SERVS (Chen et al. in prep.), where reliable environmental measurements can be performed (e.g., [Darvish et al. 2017](#)).

ACKNOWLEDGEMENTS

We thank the referee (James Aird) for the constructive comments that improved the paper. We thank James Aird, Guillermo Barro, Peter Behroozi, Francesca Civano, Iary Davidzon, and Yoshihiro Ueda for providing relevant data. We thank James Aird, Denis Burgarella, Andy Fabian, Andy Goulding, Jenny Greene, Clotilde Laigle, Jennifer Li, Amy Reines, Alexey Vikhlinin, and Feifan Zhu for helpful discussions. G.Y., W.N.B., F.V., and C.-T. J.C. acknowledge support from Chandra X-ray Center grant GO4-15130A, the Penn State ACIS Instrument Team Contract SV4-74018 (issued by the Chandra X-ray Center, which is operated by the Smithsonian Astrophysical Observatory for and on behalf of NASA under contract NAS8-03060), and the V.M. Willaman Endowment. B.L. acknowledges support from the National Natural Science Foundation of China grant 11673010 and the Ministry of Science and Technology of China grant 2016YFA0400702. M.Y.S. and Y.Q.X. acknowledge the support from the 973 Program (2015CB857004), NSFC-11473026, NSFC-11421303, the CAS Frontier Science Key Research Program (QYZDJ-SSW-SLH006), and the Fundamental Research Funds for the Central Universities. The Guaranteed Time Observations (GTO) for the CDF-N included here were selected by the ACIS Instrument Principal Investigator, Gordon P. Garmire, currently of the Huntingdon Institute for X-ray Astronomy, LLC, which is under contract to the Smithsonian Astrophysical Observatory; Contract SV2-82024. This project uses ASTROPY (a Python package; see [Astropy Collaboration et al. 2013](#)) and the SVO Filter Profile Service (<http://svo2.cab.inta-csic.es/theory/fps/>).

REFERENCES

Agol E., Krolik J. H., 2000, *ApJ*, **528**, 161
Aird J., et al., 2012, *ApJ*, **746**, 90
Aird J., Coil A. L., Georgakakis A., Nandra K., Barro G., Pérez-González P. G., 2015, *MNRAS*, **451**, 1892
Aird J., Coil A. L., Georgakakis A., 2017a, preprint, ([arXiv:1705.01132](#))
Aird J., Coil A. L., Georgakakis A., 2017b, *MNRAS*, **465**, 3390
Akylas A., Georgantopoulos I., Ranalli P., Gkiokas E., Corral A., Lanzuisi G., 2016, *A&A*, **594**, A73
Alexander D. M., et al., 2003, *AJ*, **126**, 539
Anderson M. E., Gaspari M., White S. D. M., Wang W., Dai X., 2015, *MNRAS*, **449**, 3806
Arnaud K. A., 1996, in Jacoby G. H., Barnes J., eds, *Astronomical Society of the Pacific Conference Series Vol. 101, Astronomical Data Analysis Software and Systems V*. p. 17
Astropy Collaboration et al., 2013, *A&A*, **558**, A33
Barger A. J., et al., 2003, *AJ*, **126**, 632

Baronchelli L., et al., 2017, preprint, ([arXiv:1706.06588](#))
Behroozi P. S., Wechsler R. H., Conroy C., 2013, *ApJ*, **770**, 57
Bellovary J., Brooks A., Volonteri M., Governato F., Quinn T., Wadsley J., 2013, *ApJ*, **779**, 136
Bennert V. N., Auger M. W., Treu T., Woo J.-H., Malkan M. A., 2011, *ApJ*, **742**, 107
Bongiorno A., et al., 2012, *MNRAS*, **427**, 3103
Bongiorno A., et al., 2016, *A&A*, **588**, A78
Brammer G. B., et al., 2011, *ApJ*, **739**, 24
Brandt W. N., Alexander D. M., 2015, *A&ARv*, **23**, 1
Bruzual G., Charlot S., 2003, *MNRAS*, **344**, 1000
Buchner J., et al., 2015, *ApJ*, **802**, 89
Burnham K., Anderson D., 2002, Model selection and multimodel inference: a practical information-theoretic approach, 2, 49
Calistro Rivera G., Lusso E., Hennawi J. F., Hogg D. W., 2016, *ApJ*, **833**, 98
Calzetti D., Armus L., Bohlin R. C., Kinney A. L., Koornneef J., Storchi-Bergmann T., 2000, *ApJ*, **533**, 682
Chabrier G., 2003, *ApJ*, **586**, L133
Chen C.-T. J., et al., 2013, *ApJ*, **773**, 3
Ciesla L., et al., 2015, *A&A*, **576**, A10
Cisternas M., et al., 2011, *ApJ*, **741**, L11
Civano F., et al., 2016, *ApJ*, **819**, 62
Cowie L. L., Songaila A., Hu E. M., Cohen J. G., 1996, *AJ*, **112**, 839
Croton D. J., et al., 2006, *MNRAS*, **365**, 11
Darvish B., Mobasher B., Martin D. C., Sobral D., Scoville N., Stroe A., Hemmati S., Kartaltepe J., 2017, *ApJ*, **837**, 16
Davidzon I., et al., 2017, preprint, ([arXiv:1701.02734](#))
Davis S. W., Laor A., 2011, *ApJ*, **728**, 98
Delvecchio I., et al., 2015, *MNRAS*, **449**, 373
Draine B. T., Li A., 2007, *ApJ*, **657**, 810
Elbaz D., et al., 2011, *A&A*, **533**, A119
Feldmann R., 2017, *MNRAS*, **470**, L59
Ferrarese L., 2002, *ApJ*, **578**, 90
Ferrarese L., Merritt D., 2000, *ApJ*, **539**, L9
Foreman-Mackey D., 2016, *The Journal of Open Source Software*, 1
Foreman-Mackey D., Hogg D. W., Lang D., Goodman J., 2013, *PASP*, **125**, 306
Fragos T., et al., 2013, *ApJ*, **764**, 41
Fritz J., Franceschini A., Hatziminaoglou E., 2006, *MNRAS*, **366**, 767
Gebhardt K., et al., 2000, *ApJ*, **539**, L13
Gehrels N., 1986, *ApJ*, **303**, 336
Genel S., et al., 2014, *MNRAS*, **445**, 175
Georgakakis A., Aird J., Schulze A., Dwelly T., Salvato M., Nandra K., Merloni A., Schneider D. P., 2017, preprint, ([arXiv:1705.01133](#))
Gilli R., Comastri A., Hasinger G., 2007, *A&A*, **463**, 79
Greene J. E., et al., 2016, *ApJ*, **826**, L32
Grogin N. A., et al., 2011, *ApJS*, **197**, 35
Guo Y., et al., 2013, *ApJS*, **207**, 24
Haggard D., Green P. J., Anderson S. F., Constantin A., Aldcroft T. L., Kim D.-W., Barkhouse W. A., 2010, *ApJ*, **723**, 1447
Häring N., Rix H.-W., 2004, *ApJ*, **604**, L89
Hickox R. C., Mullaney J. R., Alexander D. M., Chen C.-T. J., Civano F. M., Goulding A. D., Hainline K. N., 2014, *ApJ*, **782**, 9
Hopkins P. F., Hernquist L., 2009, *ApJ*, **698**, 1550
Hopkins P. F., Richards G. T., Hernquist L., 2007, *ApJ*, **654**, 731
Jahnke K., Macciò A. V., 2011, *ApJ*, **734**, 92
Jahnke K., et al., 2009, *ApJ*, **706**, L215
Jones M. L., Hickox R. C., Black C. S., Hainline K. N., DiPompeo M. A., Goulding A. D., 2016, *ApJ*, **826**, 12
Kelvin L. S., et al., 2014, *MNRAS*, **444**, 1647
King A., Pounds K., 2015, *ARA&A*, **53**, 115
Kocevski D. D., et al., 2012, *ApJ*, **744**, 148

- Koekemoer A. M., et al., 2011, *ApJS*, **197**, 36
- Kormendy J., Ho L. C., 2013, *ARA&A*, **51**, 511
- Laigle C., et al., 2016, *ApJS*, **224**, 24
- Lauer T. R., Tremaine S., Richstone D., Faber S. M., 2007, *ApJ*, **670**, 249
- Lehmer B. D., et al., 2016, *ApJ*, **825**, 7
- Lilly S. J., et al., 2009, *ApJS*, **184**, 218
- Liu T., et al., 2017, preprint, ([arXiv:1703.00657](https://arxiv.org/abs/1703.00657))
- Loredo T. J., 2004, in Fischer R., Preuss R., Toussaint U. V., eds, American Institute of Physics Conference Series Vol. 735, American Institute of Physics Conference Series. pp 195–206 ([arXiv:astro-ph/0409387](https://arxiv.org/abs/astro-ph/0409387)), doi:10.1063/1.1835214
- Luo B., et al., 2010, *ApJS*, **187**, 560
- Luo B., et al., 2017, *ApJS*, **228**, 2
- Lusso E., et al., 2011, *A&A*, **534**, A110
- Lusso E., et al., 2012, *MNRAS*, **425**, 623
- Marchesi S., et al., 2016a, *ApJ*, **817**, 34
- Marchesi S., et al., 2016b, *ApJ*, **830**, 100
- Marconi A., Risaliti G., Gilli R., Hunt L. K., Maiolino R., Salvati M., 2004, *MNRAS*, **351**, 169
- Martini P., Sivakoff G. R., Mulchaey J. S., 2009, *ApJ*, **701**, 66
- McCracken H. J., et al., 2012, *A&A*, **544**, A156
- McNamara B. R., Nulsen P. E. J., 2007, *ARA&A*, **45**, 117
- Merloni A., et al., 2010, *ApJ*, **708**, 137
- Mullaney J. R., et al., 2012, *ApJ*, **753**, L30
- Murtaugh P. A., 2014, *Ecology*, **95**, 611
- Noll S., Burgarella D., Giovannoli E., Buat V., Marcellac D., Muñoz-Mateos J. C., 2009, *A&A*, **507**, 1793
- Novak G. S., Ostriker J. P., Ciotti L., 2011, *ApJ*, **737**, 26
- Peng C. Y., 2007, *ApJ*, **671**, 1098
- Popping G., Caputi K. I., Somerville R. S., Trager S. C., 2012, *MNRAS*, **425**, 2386
- Rees M. J., Ostriker J. P., 1977, *MNRAS*, **179**, 541
- Reines A. E., Volonteri M., 2015, *ApJ*, **813**, 82
- Ricci C., Ueda Y., Koss M. J., Trakhtenbrot B., Bauer F. E., Gandhi P., 2015, *ApJ*, **815**, L13
- Rodighiero G., et al., 2015, *ApJ*, **800**, L10
- Rosario D. J., et al., 2013a, *ApJ*, **763**, 59
- Rosario D. J., et al., 2013b, *ApJ*, **771**, 63
- Salim S., et al., 2007, *ApJS*, **173**, 267
- Santini P., et al., 2015, *ApJ*, **801**, 97
- Schechter P., 1976, *ApJ*, **203**, 297
- Schindler J.-T., Fan X., Duschl W. J., 2016, *ApJ*, **826**, 67
- Schmidt M., 1968, *ApJ*, **151**, 393
- Schramm M., Silverman J. D., 2013, *ApJ*, **767**, 13
- Scoville N., et al., 2007, *ApJS*, **172**, 150
- Serra P., Amblard A., Temi P., Burgarella D., Giovannoli E., Buat V., Noll S., Im S., 2011, *ApJ*, **740**, 22
- Shakura N. I., Sunyaev R. A., 1973, *A&A*, **24**, 337
- Shankar F., et al., 2016, *MNRAS*, **460**, 3119
- Shemmer O., Brandt W. N., Netzer H., Maiolino R., Kaspi S., 2008, *ApJ*, **682**, 81
- Shen Y., 2013, *Bulletin of the Astronomical Society of India*, **41**, 61
- Shimizu T. T., Mushotzky R. F., Meléndez M., Koss M., Rosario D. J., 2015, *MNRAS*, **452**, 1841
- Silverman J. D., et al., 2010, *ApJS*, **191**, 124
- Sołtan A., 1982, *MNRAS*, **200**, 115
- Stanley F., et al., 2017, preprint, ([arXiv:1707.05334](https://arxiv.org/abs/1707.05334))
- Steffen A. T., Strateva I., Brandt W. N., Alexander D. M., Koekemoer A. M., Lehmer B. D., Schneider D. P., Vignali C., 2006, *AJ*, **131**, 2826
- Suh H., et al., 2017, *ApJ*, **841**, 102
- Sun M., et al., 2015, *ApJ*, **802**, 14
- Szalay A. S., Connolly A. J., Szokoly G. P., 1999, *AJ*, **117**, 68
- Tomczak A. R., et al., 2014, *ApJ*, **783**, 85
- Treister E., et al., 2009, *ApJ*, **693**, 1713
- Ueda Y., Akiyama M., Hasinger G., Miyaji T., Watson M. G., 2014, *ApJ*, **786**, 104
- Vasudevan R. V., Fabian A. C., 2007, *MNRAS*, **381**, 1235
- Vito F., et al., 2014a, *MNRAS*, **441**, 1059
- Vito F., Gilli R., Vignali C., Comastri A., Brusa M., Cappelluti N., Iwasawa K., 2014b, *MNRAS*, **445**, 3557
- Vito F., et al., 2016, *MNRAS*, **463**, 348
- Vito F., et al., 2017, preprint, ([arXiv:1709.07892](https://arxiv.org/abs/1709.07892))
- Volonteri M., 2010, *A&ARv*, **18**, 279
- Wang T., et al., 2017, *A&A*, **601**, A63
- Weigel A. K., Schawinski K., Caplar N., Wong O. I., Treister E., Trakhtenbrot B., 2017, preprint, ([arXiv:1707.05323](https://arxiv.org/abs/1707.05323))
- Xu L., Rieke G. H., Egami E., Haines C. P., Pereira M. J., Smith G. P., 2015, *ApJ*, **808**, 159
- Xue Y. Q., 2017, preprint, ([arXiv:1709.04601](https://arxiv.org/abs/1709.04601))
- Xue Y. Q., et al., 2010, *ApJ*, **720**, 368
- Xue Y. Q., Luo B., Brandt W. N., Alexander D. M., Bauer F. E., Lehmer B. D., Yang G., 2016, *ApJS*, **224**, 15
- Yang G., et al., 2017, *ApJ*, **842**, 72
- Yuan F., Narayan R., 2014, *ARA&A*, **52**, 529
- Zhang Z., Shi Y., Rieke G. H., Xia X., Wang Y., Sun B., Wan L., 2016, *ApJ*, **819**, L27

APPENDIX A: MODELING OF $P(L_{\text{SX}}|M_{\star}, z)$

We describe $P(L_{\text{SX}}|M_{\star}, z)$ at given M_{\star} and redshift with a smoothed double power law, and each parameter in this function ($\log A$, $\log L_c$, γ_1 , and γ_2) is modeled as a polynomial function of $\log M_{\star}$ and $\log(1+z)$ (see §3.3). To decide the orders of the polynomial functions, we utilize the Akaike information criterion (AIC; e.g., [Burnham & Anderson 2002](#)). The AIC technique is applicable to any log-likelihood function, and it does not assume a specific distribution of parameter uncertainties. For a given polynomial model, the AIC value is calculated as $\text{AIC} = -2 \ln L_{\text{max}} + 2k$, where k is the number of free model parameters and $\ln L_{\text{max}}$ is the maximum value of the likelihood function in Eq. 14. In L_{max} is calculated with the maximum-likelihood fitting method in §3.3. The AIC balances the complexity of the model and its efficiency in describing the data. In general, models with smaller AIC values are considered as more probable.

Assuming the currently favored model has an AIC value of AIC_F and a proposed model has an AIC value of AIC_P , we accept the proposed model as the new favored model if $\Delta\text{AIC} = \text{AIC}_P - \text{AIC}_F < \Delta\text{AIC}_T$. We choose the AIC threshold as $\Delta\text{AIC}_T = -7$ (e.g., Chapter 2.6 of [Burnham & Anderson 2002](#)). This value corresponds to a 3σ confidence level in the case when parameter uncertainties are Gaussian (e.g., [Murtaugh 2014](#)).

We first use a model of constant $\log A$, $\log L_c$, γ_1 , and γ_2 (i.e., 0th-order polynomials), and obtain $\text{AIC}_F = 24998.7$. We then test the 1st-order polynomial models of $\log A$, i.e.,

$$\log A = \log A_0 + \alpha_0^A \log(1+z) + \alpha_1^A \log M_{10}. \quad (\text{A1})$$

The fitting of the 1st-order polynomial model produces $\text{AIC}_P = 18164.2$, and thus the change of AIC is $\Delta\text{AIC} = \text{AIC}_P - \text{AIC}_F = -6834.5 < \Delta\text{AIC}_T$. Therefore, we accept the 1st-order polynomial model of $\log A$, and with this model, we further test the 1st-order models of $\log L_c$, γ_1 , and γ_2 . We find that the 1st-order models of $\log L_c$ and γ_2 significantly reduces the AIC value (< -7). Thus, γ_1 is consistent with a model that has no redshift or M_{\star} dependence.

We further test higher-order polynomial models of $\log A$

$\log L_c$, and γ_2 . The required polynomial orders for $\log A$, $\log L_c$, and γ_2 are 2nd, 2nd, and 1st, respectively. After determining the orders of the polynomials and obtaining the best-fit model parameters, we estimate the parameter uncertainties utilizing Markov chain Monte Carlo (MCMC) sampling with EMCEE (Foreman-Mackey et al. 2013).⁹ The 2D contours and 1D histograms of the sampling results are shown in Fig. A1. The 1σ confidence range of a parameter is calculated as the 16%–84% percentile range of the corresponding 1D histogram (shown as the vertical dashed lines in Fig. A1). We use the same method to derive uncertainties shown in Fig. 9. The best-fit parameters and the MCMC uncertainties are presented in Tab. 2. From Fig. A1, the contours can be highly tilted and/or irregular (e.g., β_0^L vs. α_0^L), and thus the parametric uncertainties in Tab. 2 can be strongly correlated.

APPENDIX B: $P(L_{\text{SX}}|M_\star, z)$ FITTING QUALITY

In Fig. B1, we compare the observed XLFs (§2.2) and the XLFs derived from our best-fit model (Eq. 6). The model XLFs generally agree well with the observed values. Fig. B1 also shows the observed XLFs that are not used to constrain $P(L_{\text{SX}}|M_\star, z)$ ($\log L_X < 43$; open symbols). At $z \gtrsim 0.8$, our model XLFs are consistent with the observed values at $\log L_X < 43$. At lower redshifts, our model underestimates the XLFs at $\log L_X \approx 42.5$. This underestimation might be due to the fact that our model XLFs do not include low- L_{SX} AGNs and XRBs (see 2.2).

In Fig. B2, we compare the best-fit $P(L_{\text{SX}}|M_\star, z)$ with the binned values from our sample, utilizing the $N_{\text{obs}}/N_{\text{mdl}}$ method, where N_{obs} and N_{mdl} are the observed and model-expected numbers of sources in the bin, respectively (e.g., Aird et al. 2012). Specifically, we derive the N_{mdl} from the best-fit $P(L_{\text{SX}}|M_\star, z)$ using Eq. 3. The binned $P(L_{\text{SX}}|M_\star, z)$ value is calculated as the model $P(L_{\text{SX}}|M_\star, z)$ value scaled by a factor of $N_{\text{obs}}/N_{\text{mdl}}$, while the corresponding uncertainty is the 1σ Poisson error of N_{obs} scaled by the same factor. In the bin of $z = 0.4\text{--}0.7$ and $\log M_\star = 11.5\text{--}12$ where no AGNs are detected, we derive the 1σ Poisson upper limits using the approach in Gehrels (1986). The model $P(L_{\text{SX}}|M_\star, z)$ is generally consistent with the observed values. However, we note that at $z \lesssim 1$ and $\log M_\star \gtrsim 11.5$, the constraints on $P(L_{\text{SX}}|M_\star, z)$ are weak. In this case, the $P(L_{\text{SX}}|M_\star, z)$ is largely based on model extrapolation and the uncertainties are likely underestimated.

We also compare our best-fit $P(L_{\text{SX}}|M_\star, z)$ with those derived in some previous studies in Fig. B2.¹⁰ Aird et al. (2012), Bongiorno et al. (2012), and Wang et al. (2017) adopted simple power-law models, and the slopes are (almost) independent of M_\star and redshift, similar to our results (see Tab. 2). Aird et al. (2012) and Wang et al. (2017) probed $\log(L_{\text{SX}}) \lesssim -0.5$; their slopes are ≈ 0.4 and ≈ 0.6 , respectively, similar to the low- L_{SX} slope in our model. Their normalizations are dependent on redshift but not M_\star , while

our normalization depends on both factors. Therefore, their normalizations should be considered as averaged over the M_\star range of their samples. The relatively flat power-law shape at low-to-moderate L_{SX} is also confirmed by two recent studies (Aird et al. 2017a; Georgakakis et al. 2017) that adopt non-parametric modeling for $P(L_{\text{SX}}|M_\star, z)$.¹¹ These two studies also identified a sharp drop of $P(L_{\text{SX}}|M_\star, z)$ above $\log L_{\text{SX}} \approx 0$, similar to our results. Bongiorno et al. (2012) obtained a steeper slope (≈ 1.0); the reason could be that they probed L_{SX} above the break L_{SX} , where the slope is steep (≈ 2.5 in our model; see Tab. 2). Thus, it is understandable that their slope is between our low- L_{SX} and high- L_{SX} slopes. Bongiorno et al. (2016) modeled the bivariate distribution function of M_\star and redshift, i.e., $\Psi(L_{\text{SX}}, M_\star, z)$, and we convert it to $P(L_{\text{SX}}|M_\star, z)$ by dividing it by our adopted SMF (§2.2). The resulting $P(L_{\text{SX}}|M_\star, z)$ shape is also a double power law. Their low- L_{SX} slope depends on redshift and is steeper than our low- L_{SX} slope at $z \lesssim 1.5$. From our data, it appears Bongiorno et al. (2016) overestimated the low- L_{SX} slope. A possible reason for this difference might be that they did not include the ultradeep fields (GOODS-S and GOODS-N) that are critical in constraining the low- L_{SX} slope.

This paper has been typeset from a $\text{\TeX}/\text{\LaTeX}$ file prepared by the author.

⁹ <http://dan.iel.fm/emcee/current/>

¹⁰ We do not compare with the studies that investigate λ_{Edd} distributions (e.g., Hopkins & Hernquist 2009; Weigel et al. 2017), since it is not feasible to convert their λ_{Edd} distribution to $P(L_{\text{SX}}|M_\star, z)$.

¹¹ The results of $P(L_{\text{SX}}|M_\star, z)$ in Aird et al. (2017a) and Georgakakis et al. (2017) are not publicly available. Therefore, their $P(L_{\text{SX}}|M_\star, z)$ curves are not shown in Fig. B2.

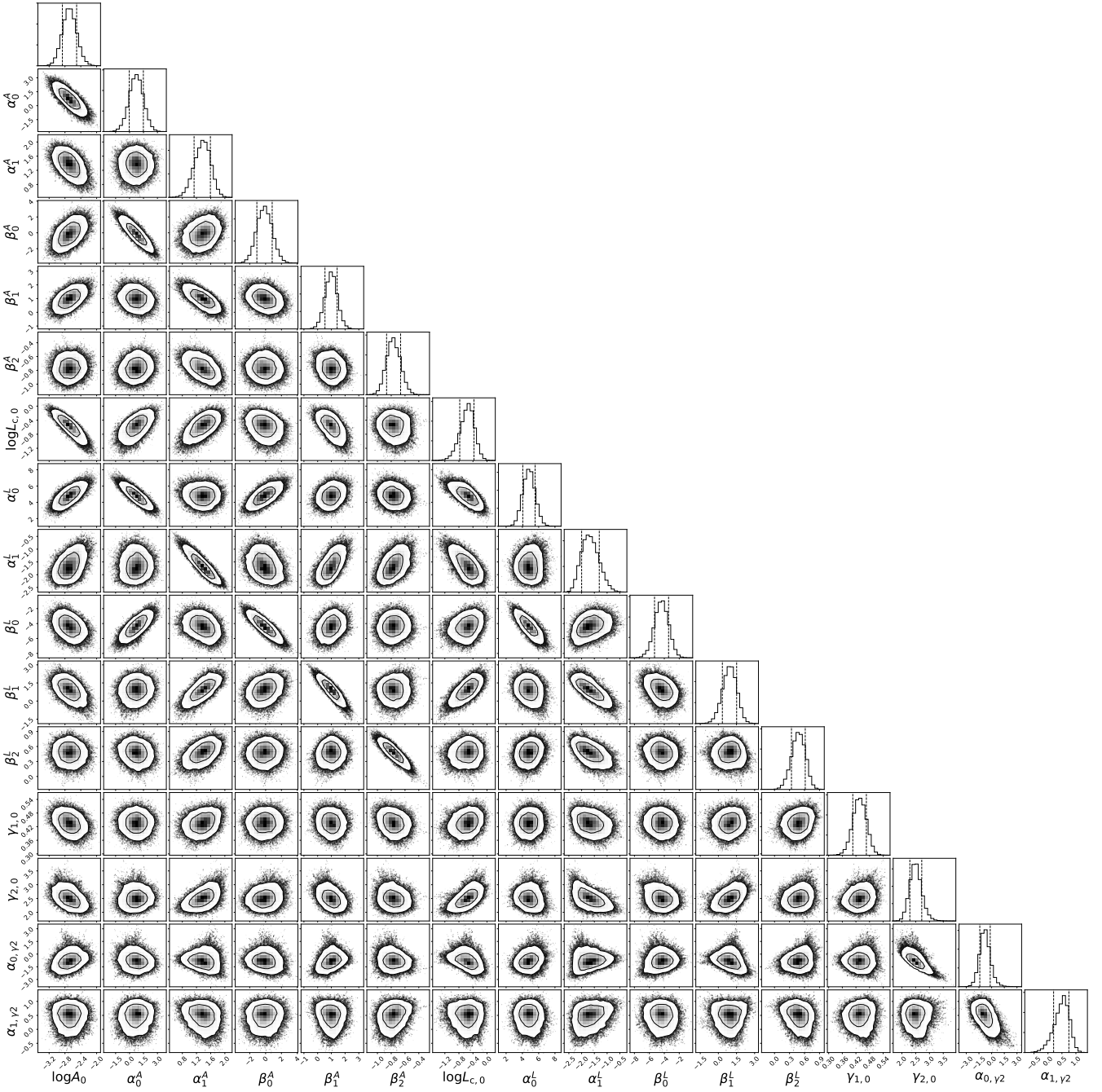


Figure A1. 2D contours and 1D histograms for our MCMC sampling results. The vertical dashed lines in the histograms indicate the 1σ confidence intervals. The contour confidence levels are 1σ (68.3%) and 2σ (95.5%), respectively. The grayscale pixels inside the 1σ contour denote probability with darkened color indicating higher probability. The points outside the 2σ contour represent individual MCMC sampling. This figure is plotted using CORNOR.PY (Foreman-Mackey 2016). Some contours are highly irregular/tilted, indicating strongly correlated parametric uncertainties.

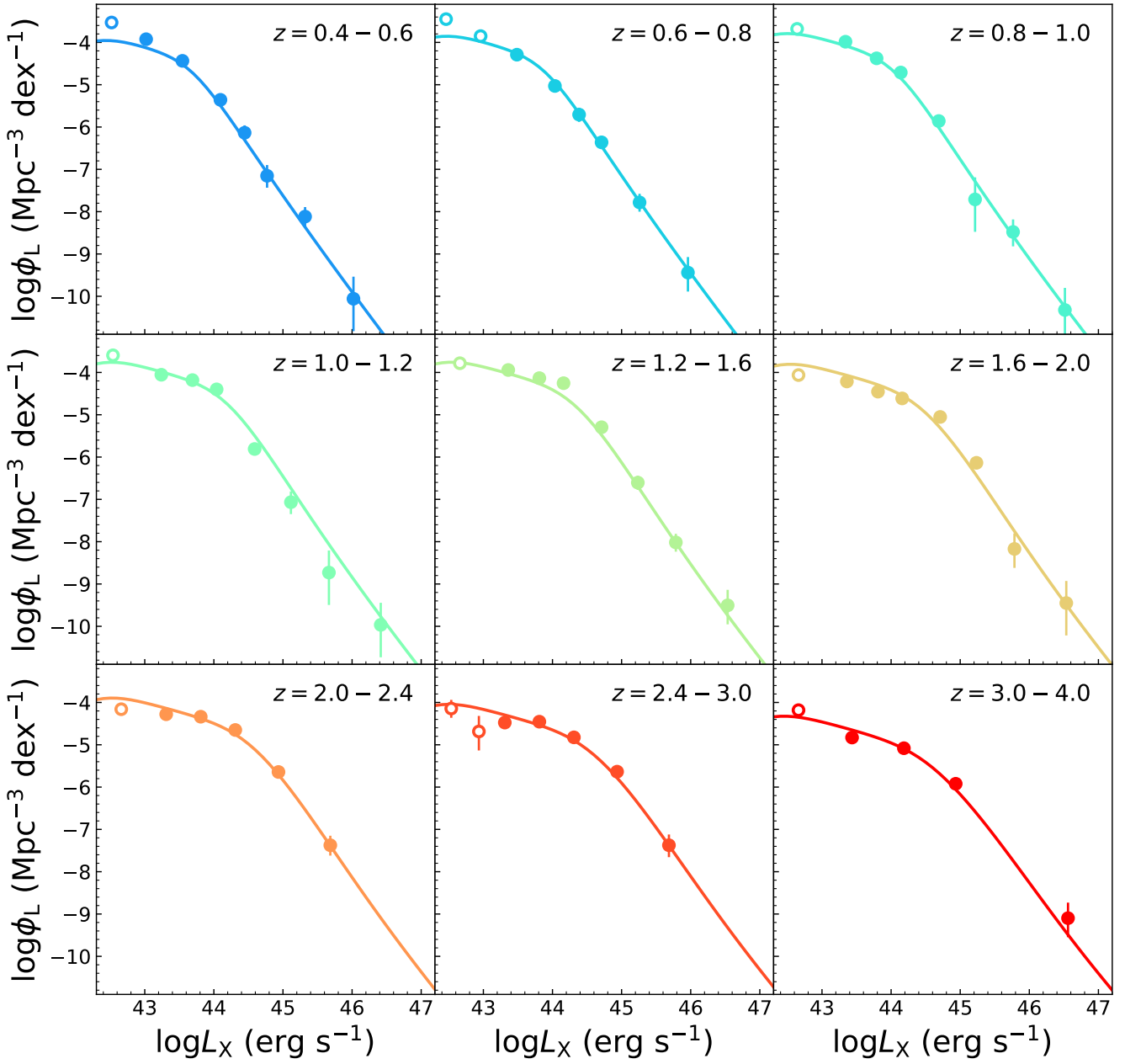


Figure B1. The XLFs in redshift bins from $z = 0.4$ – 4 . The solid curves are the XLFs derived from our best-fit $P(L_{\text{SX}}|M_\star, z)$ model. The data points indicate the soft-band XLFs from Ueda et al. (2014). The solid symbols represent the XLFs used in this work; the open symbols represent the XLFs below our L_X threshold (see §2.2). The XLFs from our model fit the observed data acceptably in general.

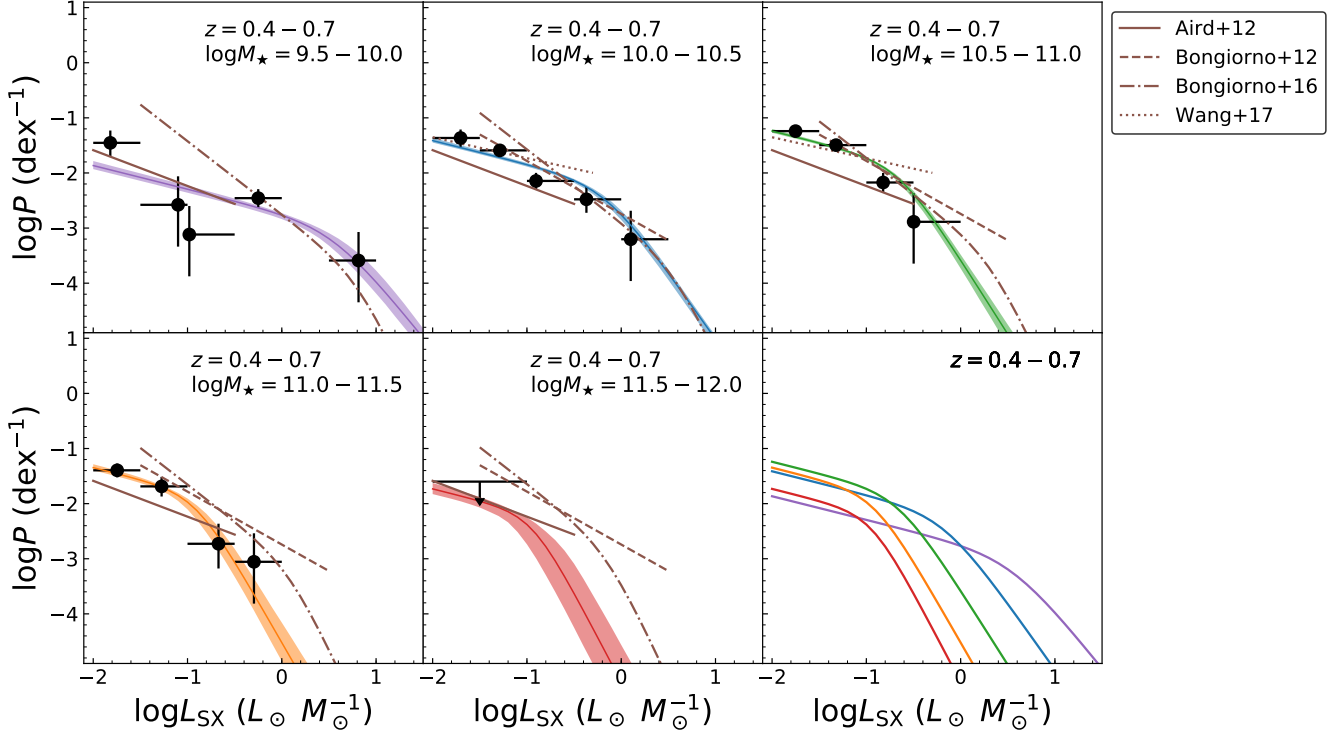


Figure B2. $P(L_{\text{SX}}|M_{\star}, z)$ for different M_{\star} and redshift ranges. The solid curves with blue, orange, green, red, and purple colors indicate our best-fit $P(L_{\text{SX}}|M_{\star}, z)$ model, and the shaded regions indicate the 1σ confidence intervals. For each of the seven redshift ranges, the first five panels display the probability distributions for five M_{\star} ranges; the last panel compares our best-fit $P(L_{\text{SX}}|M_{\star}, z)$ for these M_{\star} ranges. The data points indicate the binned $P(L_{\text{SX}}|M_{\star}, z)$ values from our sample. The error bars (upper limit) indicate the Poisson 1σ confidence level. The brown curves represent $P(L_{\text{SX}}|M_{\star}, z)$ from the literature. Our best-fit model is in agreement with the data. The brown lines indicate $P(L_{\text{SX}}|M_{\star}, z)$ from different studies. Here, we only present the figures for $z = 0.4-0.7$ and $z = 1.0-1.5$ for display purposes; the entire set of 6 figures for the other redshift ranges is available in the online version of the journal.

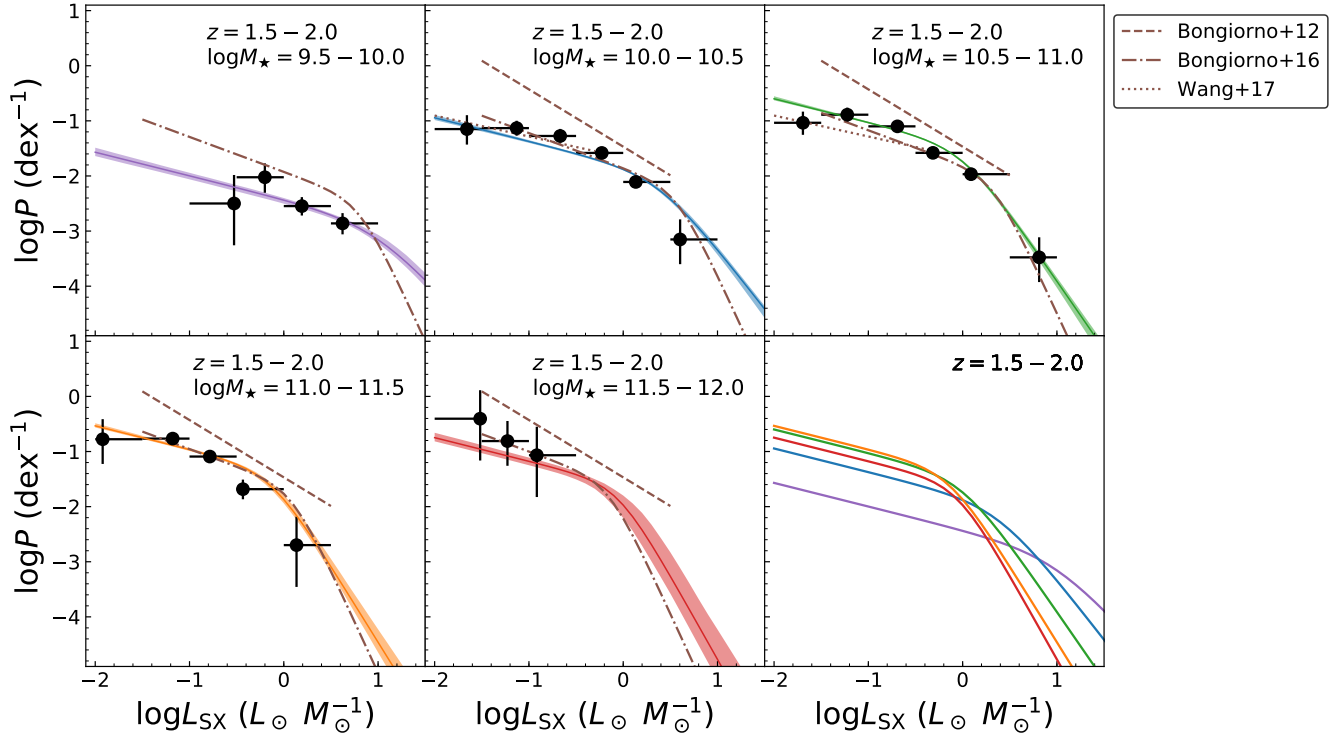


Figure B2 – continued